

Experimental Study on the Seismic Mitigation Performance of Metafoundations on a Uniform Soil Layer

Lei Xiao, Feifei Sun, Oreste S. Bursi, Heng Li & Meng Wang

To cite this article: Lei Xiao, Feifei Sun, Oreste S. Bursi, Heng Li & Meng Wang (2023) Experimental Study on the Seismic Mitigation Performance of Metafoundations on a Uniform Soil Layer, Journal of Earthquake Engineering, 27:14, 4206-4236, DOI: [10.1080/13632469.2022.2162632](https://doi.org/10.1080/13632469.2022.2162632)

To link to this article: <https://doi.org/10.1080/13632469.2022.2162632>



Published online: 06 Jan 2023.



Submit your article to this journal 



Article views: 170



View related articles 



View Crossmark data 



Citing articles: 1 View citing articles 



Experimental Study on the Seismic Mitigation Performance of Metafoundations on a Uniform Soil Layer

Lei Xiao^{a,b}, Feifei Sun^a, Oreste S. Bursi^c, Heng Li^b, and Meng Wang^d

^aState Key Laboratory of Disaster Reduction in Civil Engineering, Tongji University, Shanghai, China; ^bDepartment of Building and Real Estate, Hong Kong Polytechnic University, Hong Kong; ^cDepartment of Civil, Environmental and Mechanical Engineering, University of Trento, Trento, Italy; ^dKey Laboratory of Urban Security and Disaster Engineering of Ministry of Education, Beijing University of Technology, Beijing, China

ABSTRACT

The seismic mitigation performance of a metafoundation with soil-structure interaction was investigated utilizing shaking table tests. The results indicated that the metafoundation's performance strongly depended on the coupling among the frequencies of the soil layer, structural systems, and input motions. Due to resonant effects, the response of the controlled structure could be greater than that of the uncontrolled superstructure at small input PGAs. By contrast, the metafoundation exhibited excellent mitigation effects at large PGAs. A simplified elastic model was validated by the experimental results. Then the validated model contributed to the interpretation of experimental phenomena based on equivalent linear parameters.

ARTICLE HISTORY

Received 18 May 2022

Accepted 19 December 2022

KEYWORDS

Soil-structure interaction; metafoundation; shaking table test; time-frequency representation; simplified model

1. Introduction

Due to their strong wave attenuation ability in specific frequency ranges, metamaterials provide new solutions to existing vibration problems. The frequency ranges where wave propagation is forbidden are called band gaps. To date, applications of metamaterials to isolate structural vibrations caused by earthquakes (Achaoui et al. 2015; Casablanca et al. 2018; Cheng et al. 2020; Sun et al. 2021, 2020), traffic loads (Pu and Shi 2020; Pu, Shi, and Xiang 2018), and machine vibrations (Ujjawal, Venkateswarlu, and Hegde 2019) have been explored. For vibration isolation, two types of applications have been proposed so far based on wave types: metafoundations which are designed to counteract the effects of body waves utilizing mechanical filtering; and metabarriers that are conceived to mitigate surface wave effects on foundation by means of wave diversion.

In the past decade, a few researchers have reported the feasibility of ground vibration mitigation by means of metafoundations constructed with common engineering materials. Usually, the composite cells of metafoundations consist of a continuous host material with a matrix of resonators inside. The bandwidth and the attenuation effect in the band gap are directly proportional to the mass ratio of resonators to the host material and the compliance of the host material (2023). To reduce the mass and stiffness of the host material, which can benefit a wide band gap with clear attenuation effects at a reduced price, La Salandra et al. proposed a novel type of metafoundation by replacing the continuous host material with a shear frame (La Salandra et al. 2017). Following their work, the metafoundation was optimized in the frequency and time domain to evaluate its ability to reduce fuel storage tanks for site-specific seismic hazards (Basone et al. 2019; Sun, Xiao, and Bursi 2019). Wenzel et al. investigated the performance enhancement of the metafoundation with nonlinear negative stiffness elements (Wenzel, Bursi, and Antoniadis 2020). Furthermore, the metafoundation was designed to protect tanks against both horizontal and vertical ground accelerations (Franchini et al.

2020). Two types of metafoundations, i.e. i) a foundation endowed with resonators and linear dampers tuned to multiple frequencies, and ii) a foundation equipped with resonators and fully nonlinear hysteretic devices, were designed to provide favorable properties in the ultra-low-frequency regime (Bursi, Basone, and Wenzel 2021).

Starting from the ground with boreholes (Brùlé et al. 2014), metabarriers have grown simultaneously on the field of resonators buried in the ground (Pu and Shi 2018) and above the ground (Colombi, Colquitt et al. 2016). A novel application of employing forests as natural metabarriers was proposed by Colombi, Colquitt et al. (2016); they demonstrated by means of FE simulations that a Rayleigh wave would experience strong attenuation when interacting with a forest (Colombi, Colquitt et al. 2016; Colombi, Roux et al. 2016). Following their work, to validate the effect of periodically planted trees on vibration control, both a 3D simulation model and experimental tests were applied; moreover, the influence of soil elastic modulus, tree height, trunk diameters, and tree distances on band gaps were investigated (Huang, Liu, and Li 2019; Liu et al. 2019). Muhammad et al. investigated the feasibility of the application of periodically arranged built-up steel sections as resonant barriers for mitigating seismic waves (Lim and Reddy 2019). The interested reader can find in (Brùlé, Enoch, and Guenneau 2020) and (Mu et al. 2020) thorough reviews of research on seismic mitigation applications of metamaterials.

Soil-structure interaction (SSI) represents a crucial issue in the evaluation of the seismic mitigation performance of metabarriers and metafoundations. More specifically, SSI is certainly considered in the research on metabarriers buried in the soil or built near the soil surface. In this respect, to show the practical feasibility of seismic metabarriers, a large-scale in situ experiment was carried out by Brùlé et al (Brùlé et al. 2014). From a simulation viewpoint, Colombi, Roux et al. (2016) employed FE models with perfectly layer conditions applied on the boundaries of a halfspace. Geng et al. (Geng, Zhu, and Chong 2018) investigated the performance of a 1D metabarrier embedded in soil by means of FE models, in which 2500 m-long segments were connected to both ends of the metabarrier. Conversely, Palermo et al. (Palermo et al. 2016; Palermo, Vitali, and Marzani 2018), by means of an analytical model able to capture the relevant interaction, investigated the interaction between the dynamic mass of soil and the moving mass of buried resonators. They then verified analytical results by FE simulations and a small-scale experiment (Palermo et al. 2016; Palermo, Vitali, and Marzani 2018). To model the soil-resonator interaction of a buried metabarrier, Wagner et al. (Wagner et al. 2018) employed a linear spring endowed with a frequency-independent stiffness. Moreover, to address uncertainties of both the excitation and system properties, a robust-to-uncertainties optimization process was carried out. Pu et al. derived the dispersive properties of Rayleigh waves propagating in fully saturated or layered porous media equipped with surface mass-spring resonators (Pu et al. 2020).

To the best of the knowledge of the authors, publications on metafoundations with SSI included are scarce. Shi and Huang verified the feasibility of a buried metafoundation with a 3D soil-foundation FE model (Shi and Huang 2013). Sun et al., instead, investigated the influence of SSI on the seismic mitigation performance of a type of metafoundation based on mechanical models; as a result, a more favorable vibration mitigation effect was achieved when the SSI was taken into account (Sun, Xiao, and Bursi 2020). Such conclusions are primarily theoretically based and refer to elastic behaviors, thus requiring further investigations and generations. Laboratory investigations are essential for studying the complex SSI effect (Anastasopoulos et al. 2013). Along with analytical simulations, laboratory investigations are pivotal for understanding the seismic response of soil-metafoundation-superstructure systems.

Along this vein, the scope of the present work is to examine the seismic mitigation performance of metafoundations with SSI based on shaking table tests. The objectives are i) to verify the capability of a simplified approach to model the global behavior of soil-metafoundation-superstructure systems at the elastic stage, and ii) to examine the vibration mitigation effect with SSI at different excitation levels. Thus, the paper is organized as follows. Methodologies and formulations used to investigate the SSI of superstructures with and without a metafoundation are presented in Section 2. The shaking table test programs are introduced in Section 3. Section 4 deals with the comparison of numerical and test

results as well as the discussion on the impact of SSI. Section 5 summarizes the work carried out and provides both conclusions and future developments.

2. Description of the Controlled and Uncontrolled Systems

2.1. Problem Description

The shear-frame-based metafoundation, which can benefit from stiffness reduction of the host material, is designed for the attenuation of the impulsive mode of a slender tank (Basone et al. 2019; Sun, Xiao, and Bursi 2019), as shown in Fig. 1. The sketch of the superstructure-metafoundation system on a soil layer is shown in Fig. 2a. Works in this study is a pioneering effort towards understanding the influence of SSI on the performance of metafoundations. The SSI in the case where metafoundations are embedded in the soil layer is complicated. Hence, a gap is set between the metafoundation and surrounding soil as a reasonable solution, which is also adopted in most applications of traditional rubber bearings (Kumar and Saha 2021) and metafoundations (Colombi et al. 2020; Liu, Wang, and Chen 2019; Martakis et al. 2021). The corresponding dynamic model is displayed in Fig. 2b, in which the superstructure is further simplified as a single-degree-of-freedom (SDoF) structure representing the impulsive mode, and only the soil-structure interaction at the bottom is considered. The metafoundation modeling is carried out by condensing both masses and stiffness of each layer. The superstructure-metafoundation system is denoted as the controlled system hereafter. The superstructure with a fixed base for comparison is denoted as the uncontrolled system. The modeling of the controlled and uncontrolled systems on a uniform homogeneous elastic soil layer is introduced in the following subsections.

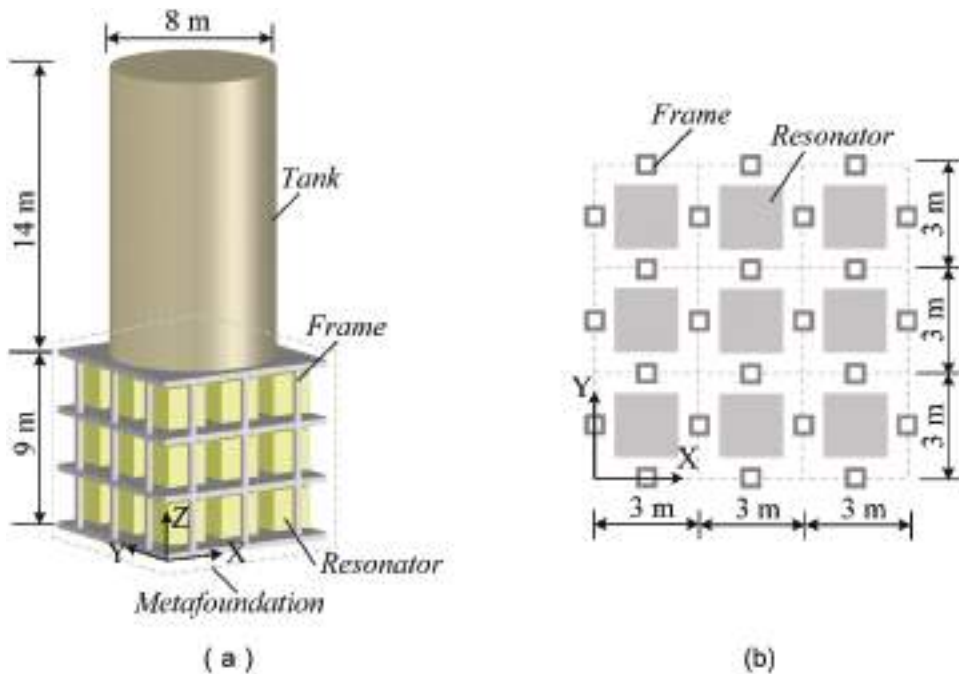


Figure 1. Coupled foundation-tank system in (Basone et al. 2019; Sun, Xiao, and Bursi 2019). (a) Isometric view; (b) plan view.

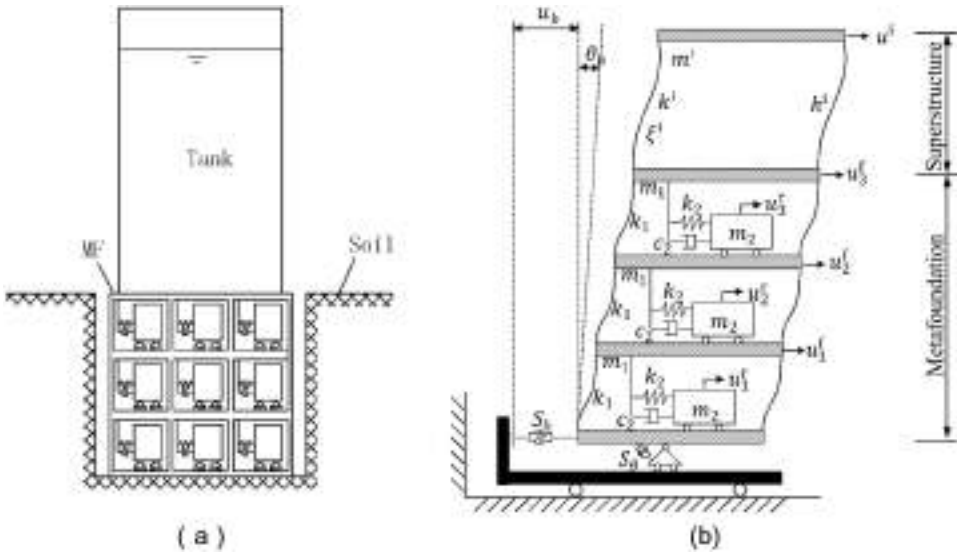


Figure 2. The controlled system on a soil layer. (a) tank and metafoundation (MF) and (b) dynamic model.

2.2. Modeling of the Uncontrolled System

In the case of soil Poisson's ratio $\nu \leq 1/3$, the simplified model of the uncontrolled superstructure is shown in Fig. 3 (Livaoglu 2008). The rigid massless foundation is attached to the uniform soil layer below by two sets of springs, one set for horizontal motion S_h and one set for rotational motion S_θ . The dynamic stiffnesses of these two springs are frequency-dependent and are calculated from the static stiffness K_j , the dynamic spring coefficient $k_j(a_0)$, and the dynamic damping coefficient $c_j(a_0)$ as

$$S_j(a_0) = K_j(k_j(a_0) + ia_0c_j(a_0)) \quad (j = h, \theta) \quad (1)$$

For simplicity, the parameters and equations to calculate the dynamic stiffnesses are provided in Appendix A1.

The total displacement is given by

$$u_t = u_{ff}(0, t) + u_b + h^i \theta_b + u \quad (2)$$

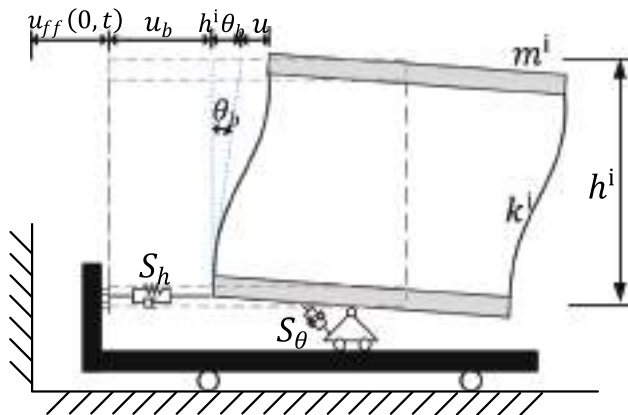


Figure 3. Dynamic model of the uncontrolled superstructure with SSI used for both horizontal and rocking motions with $\nu \leq 1/3$ (Livaoglu 2008).

where the terms in Eq. (2) are defined in Fig. 3.

Then, the dynamic equilibrium of the system can be formulated as

$$\mathbf{A}\mathbf{u}^{\text{unc}} = u_{ff0}(\omega)\mathbf{I}_1 \tag{3}$$

with

$$\mathbf{A} = \begin{bmatrix} \frac{\omega_i^2}{\omega^2}(1 + 2i\xi^i) - 1 & -1 & -1 \\ -1 & \frac{S_b(a_0)}{m\omega^2} - 1 & -1 \\ -1 & -1 & \frac{S_\theta(a_0)}{m^i(h^i)^2\omega^2} - 1 \end{bmatrix} \tag{4}$$

$$\mathbf{u}^{\text{unc}} = [u(\omega) \ u_b(\omega) \ h^i\theta_b(\omega)]^T \tag{5}$$

$$\mathbf{I}_1 = [111]^T \tag{6}$$

$\omega_i \left(= \sqrt{\frac{k^i}{m^i}} \right)$ defines the fixed-base natural frequency of the superstructure, ξ^i is the damping ratio of the superstructure, and the superscript “unc” in Eq. (5) means uncontrolled.

The displacement transfer function of each degree of freedom can be calculated by replacing $u_{ff0}(\omega)$ in Eq. (3) with one unit:

$$\mathbf{u}^{\text{unc}} = \mathbf{A}^{-1}\mathbf{I}_1 \tag{7}$$

Then, the absolute acceleration transfer function of the superstructure can be obtained as:

$$H(i\omega) = 1 + u(\omega) + u_b(\omega) + h^i\theta_b(\omega) \tag{8}$$

Then, by introducing the transfer function of the soil layer $R(i\omega)$ (see Appendix A2), the transfer function of the soil-uncontrolled superstructure system can be expressed as:

$$H_{\text{unc}}(i\omega) = R(i\omega)H(i\omega) \tag{9}$$

2.3. Modeling of the Passive Controlled System

The passive controlled system is shown in Fig. 2b. More precisely, the metafoundation is simplified as a linear-elastic frame with multi-inner resonators. Similar to the uncontrolled system, the base is connected to the soil below by two sets of springs. The system of equations of motion of a controlled system with a 3-cell metafoundation can be expressed as:

$$\mathbf{M}^{\text{con}}\ddot{\mathbf{u}}^{\text{con}} + \mathbf{C}^{\text{con}}\dot{\mathbf{u}}^{\text{con}} + \mathbf{K}^{\text{con}}\mathbf{u}^{\text{con}} = -m\ddot{u}_{ff0}(\omega) \tag{10}$$

in which

$$\mathbf{u}^{\text{con}} = [u_1^f \ u_2^f \ u_3^f \ u_1^r \ u_2^r \ u_3^r \ u^i \ u_b \ \theta_b]^T \tag{11}$$

As shown in Fig. 2, u_j^f , u_j^r and u^i ($j = 1, 2, 3$) denote the relative displacement of each DoF to the displacement of the base plate. u_b denotes the relative displacement of the base plate to the ground motion and θ_b defines the rotational DoF. Details of system matrices are given in Appendix.

Due to a harmonic excitation $\ddot{u}_{ff0}(t)$ of the form $e^{i\omega t}$, the transfer function (TF) relating the relative displacement of the system to the excitation reads

$$\mathbf{H}_u(i\omega) = \frac{-m}{-\omega^2\mathbf{M}^{\text{con}} + i\omega\mathbf{C}^{\text{con}} + \mathbf{K}^{\text{con}}} \tag{12}$$

and the transfer function of the absolute acceleration of the controlled superstructure can be expressed as

$$H_a(i\omega) = 1 - \omega^2(\mathbf{H}_u(7) + \mathbf{H}_u(8) + \mathbf{H}_u(9) \times h_4) \tag{13}$$

in which $\mathbf{H}_u(7)$, $\mathbf{H}_u(8)$ and $\mathbf{H}_u(9)$ are the components corresponding to u^i , u_b , and θ_b , respectively. h_4 is the distance between the top of superstructure and the base plate.

Then similarly, the transfer function of the controlled system fixed at the surface of a soil layer can be expressed as

$$H_{con}(i\omega) = R(i\omega)H_a(i\omega) \tag{14}$$

2.4. Properties of a Periodic Lattice

The prototype is the condensed model of a three-cell periodic foundation investigated in previous research (Sun, Xiao, and Bursi 2019). The parameters of the prototype are displayed in Table 1. If the metafoundation can be designed as an infinite periodic system, as shown in Fig. 4, then the system can suppress the propagation of waves in certain frequency ranges, which are called band gaps. The band gaps can be solved by means of dispersion analysis using the Floquet-Bloch theorem (Basone et al. 2019). Motion equations for the j^{th} unit cell of the metafoundation are as follows:

$$m_1 \ddot{u}_j^f + k_1 (2u_j^f - u_{j-1}^f - u_{j+1}^f) + k_2 (u_j^f - u_j^r) = 0 \tag{15}$$

$$m_2 \ddot{u}_j^r - k_2 (u_j^f - u_j^r) = 0 \tag{16}$$

For Eq. (15) and (16), the generalized form of the Floquet-Bloch theorem is applied

$$u_{j\pm 1}^m = e^{\pm i\kappa h_c + \lambda t} U^m \tag{17}$$

where $m = f$ and r is the index of the considered mass; $\pm h_c$ is the distance from the reference j^{th} cell to the considered $j^{th} \pm 1$ cell; U^m is the wave motion amplitude. κ is wave number and in the absence of damping, $\lambda = i\omega$. Substituting Eq. (17) into Eq. (15) and (16) leads to the well-known eigenvalue

Table 1. Properties and scale factors of the condensed prototype and model.

Type	Physical quantity	Prototype	Model	Scale factor (Model/Prototype)
Mass (kg)	m_1	73060.00	0.84	1.15E-05
	m_2	169290.00	1.95	1.15E-05
	m^i	507882.43	5.84	1.15E-05
Stiffness (N/m)	k_1	599000000.00	27540.23	4.60E-05
	k_2	272000000.00	1250.57	4.60E-05
	k^i	845300000.00	38860.80	4.60E-05
Length (m)	h_c	3.00	0.20	6.67E-02
	H	27.00	1.80	6.67E-02
Frequency (Hz) and time (s)	f_1	6.49	12.99	2.00E+00
	f_2	2.02	4.03	2.00E+00
	f_{soil}	4.40	8.80	2.00E+00
Time step		\	\	5.00E-01

Notes: h_c -Height of frame columns.

H- Thickness of the soil layer;

f_1 - The fixed-base natural frequency of the superstructure; $f_1 = \sqrt{k^i/m^i}/(2\pi) = \omega_i/(2\pi)$

f_2 - The natural frequency of resonators; $f_2 = \sqrt{k_2/m_2}/(2\pi)$

f_{soil} - The natural frequency of the soil layer;

Other terms are defined in Fig. 2b.

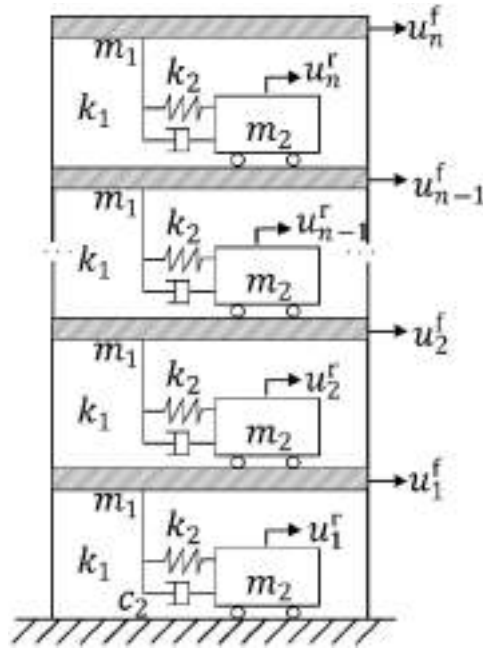


Figure 4. One-dimensional mass-resonator chain model.

problem. The non-trivial solution of the eigenvalue problem yields the following dispersion relationship:

$$m_1 m_2 \omega^4 - ((m_1 + m_2)k_2 + 2m_2 k_1 (1 - \cos(\kappa h_c)))\omega^2 + 2k_1 k_2 (1 - \cos(\kappa h_c)) = 0 \quad (18)$$

Then, Fig. 5 illustrates the dispersion relation and corresponding band gap of an infinite periodic stack of the same unit cell of the metafoundation. Clearly, a band gap forms in the frequency

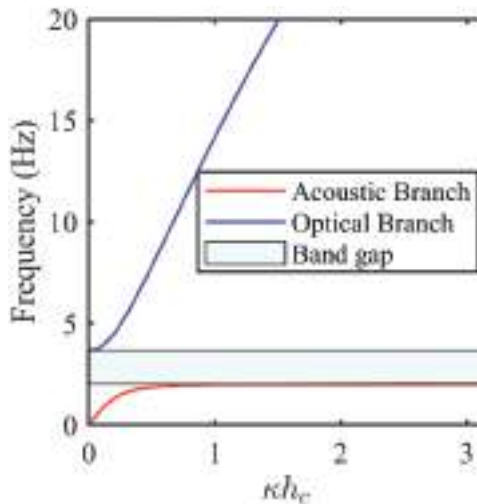


Figure 5. Dispersion relation for an infinite stack of unit cells with the geometric properties of the studied metafoundation.

range of (2.02, 3.67) Hz, which does not allow the propagation of elastic waves. However, this result is only valid for an infinite lattice. Additional analyses are presented hereinafter for the case of a finite metafoundation.

3. Shaking Table Test Program

3.1. Shaking Table Testing Facility

The shaking table equipment adopted for the experimental activities was a six-degree-of-freedom shaking table (4×4 m) belonging to the State Key Laboratory for Disaster Reduction in Civil Engineering, Tongji University. The working frequency ranges from 0.1 to 50 Hz. The shaking table vibrates with two maximum horizontal accelerations of 1.2 g and 0.8 g, respectively, and a maximum vertical acceleration of 0.7 g, with a maximum payload of 15 tons.

To minimize the box effect, a flexible cylindrical container, which has been extensively used in several shaking table tests (Chen et al. 2016; Li, Yang, and Lu 2018), was employed. The cylindrical soil container is endowed with a 3-meter diameter, as indicated in Fig. 6.

3.2. Structure Model

The typical problem with small-scale modeling lies in its limited ability to satisfy physical and geometrical similarity laws between the model and the prototype. However, the effectiveness depends on whether the main factors influencing the behavior of the prototype are captured in the model (Durante et al. 2016). Tests in this work aim to assess the SSI effect on the seismic mitigation effect of a metafoundation in terms of global system responses. The seismic mitigation effect depends on the mass and frequency ratios among the three components: the superstructure, the inner resonator, and the metafoundation's outer frame. The vibration mitigation effect also depends on the total number of cells. In this study, all these factors of the model are the same as those of the prototype. Hence, the model can reflect the main behavior of the prototype. The scaling factors of the model to the prototype are summarized in Table 1. Note that the frequency ratio between the model and the prototype is two. Hence, due to similitude constraints, the time steps of the selected accelerograms are scaled down by 0.5.

The fabricated model of the controlled system is schematically shown in Fig. 7, which consists of the SDoF superstructure and the three-layered metafoundation. Each unit cell of the metafoundation is composed of an outer frame and an inner resonator, which is connected to the outer frame by steel strips. The photos of the controlled and uncontrolled models are shown in Fig. 8. Geometric parameters of columns of outer frames, steel strips, and masses are determined according to the parameters of the condensed model in Table 1.

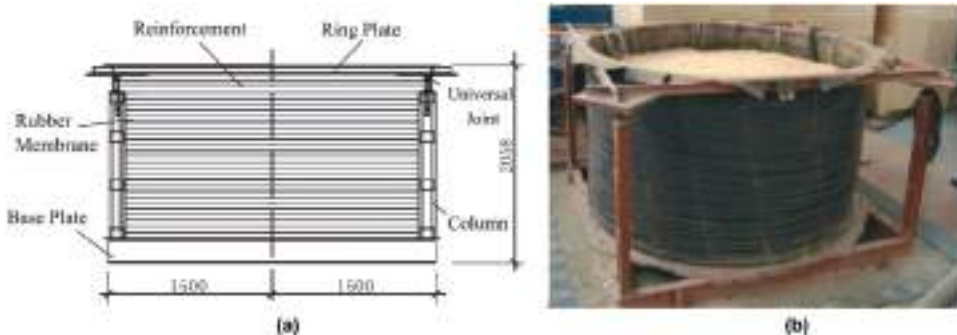


Figure 6. (a) schematic diagram (mm) and (b) photo of the flexible soil container.

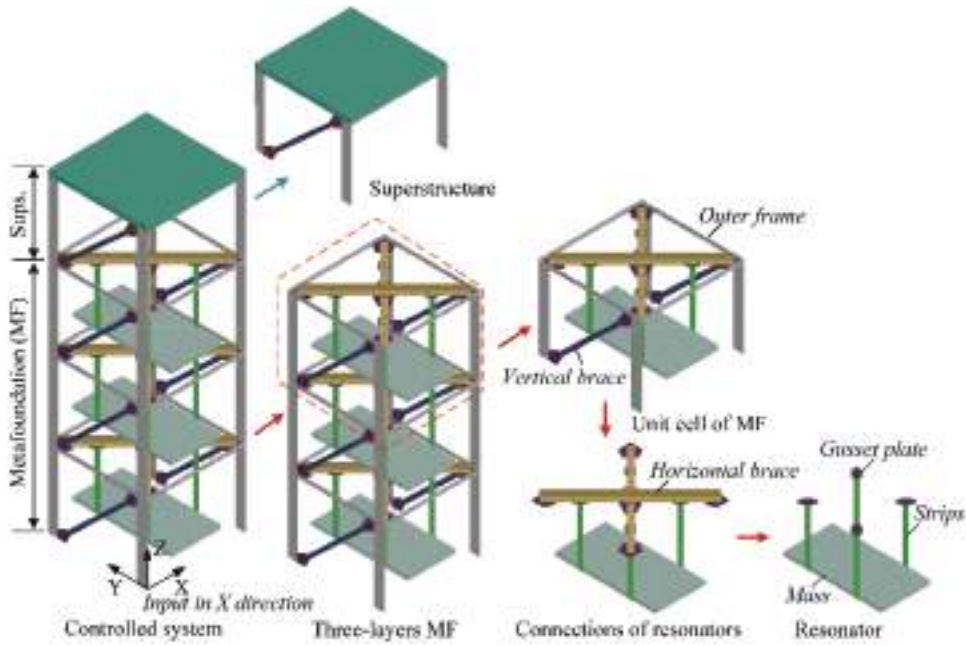


Figure 7. Exploded diagram of the controlled model.



(a) The controlled model



(b) The uncontrolled model

Figure 8. Photos of (a) the controlled system and (b) the uncontrolled system at the surface of soil layer.

In this study, only the SSI at the bottom is considered. Hence, the controlled and uncontrolled models were fixed on the top of the soil layer shown in Fig. 8. The plan view of the arrangement of the controlled and uncontrolled models can be found in Fig. 9. These two models were arranged in a plane perpendicular to the excitation direction so that the interaction between the two models was negligible. The distance of each model to the boundary of the flexible container was 600 mm. Previous

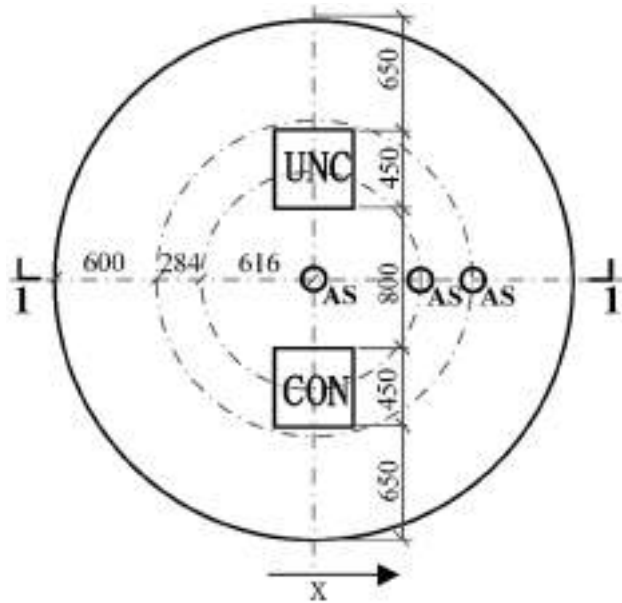


Figure 9. Plan view of the arrangement of the uncontrolled and controlled superstructure on the top of the soil layer.

investigations have shown that the boundary effect can be ignored when the distance between the structure and the boundary is no less than 600 mm (Lu et al. 2004). Hence, the boundary effect could be ignored.

3.3. Model Soil

A mixture of sand and sawdust was used as the model soil in the test. The soil profile was one uniform layer with a 1.8 m depth. The model soil was designed with mass density ρ equal to $700\text{kg}/\text{m}^3$. The corresponding tested shear modulus is 2.84 MPa. Then the design eigenfrequency of the soil layer was 8.8 Hz. However, the eigenfrequency obtained by the experimental soil deposition procedure was somewhat different from the target value (see Subsection 4.1).

3.4. Instrumentation

For measurement purposes, i.e. to characterize the dynamic response of the model structures as well as soil, three types of sensors were used:

- accelerometers: with labels starting with “AC” when located on the controlled system, “AU” when located on the uncontrolled system, and “AS” when in the soil;
- displacement meters: with labels starting with “DC” when on the controlled system and “DU” when on the uncontrolled system;
- strain gauges: with labels starting with “S.”

For the sake of clarity, Fig. 10 shows the instrumentation arrangement for the controlled system. In particular, the accelerometers AC #1–5 were used to measure the in-plane acceleration response of each floor. Displacement meters DC #1–3 were used to capture the in-plane displacement of the superstructure, the top of the metafoundation, and the base slab, respectively. A similar instrumentation arrangement for the uncontrolled system can be seen in Fig. 11. At the same time, Fig. 12 shows the arrangement of accelerometers buried in the soil layer. In particular, there were three groups of

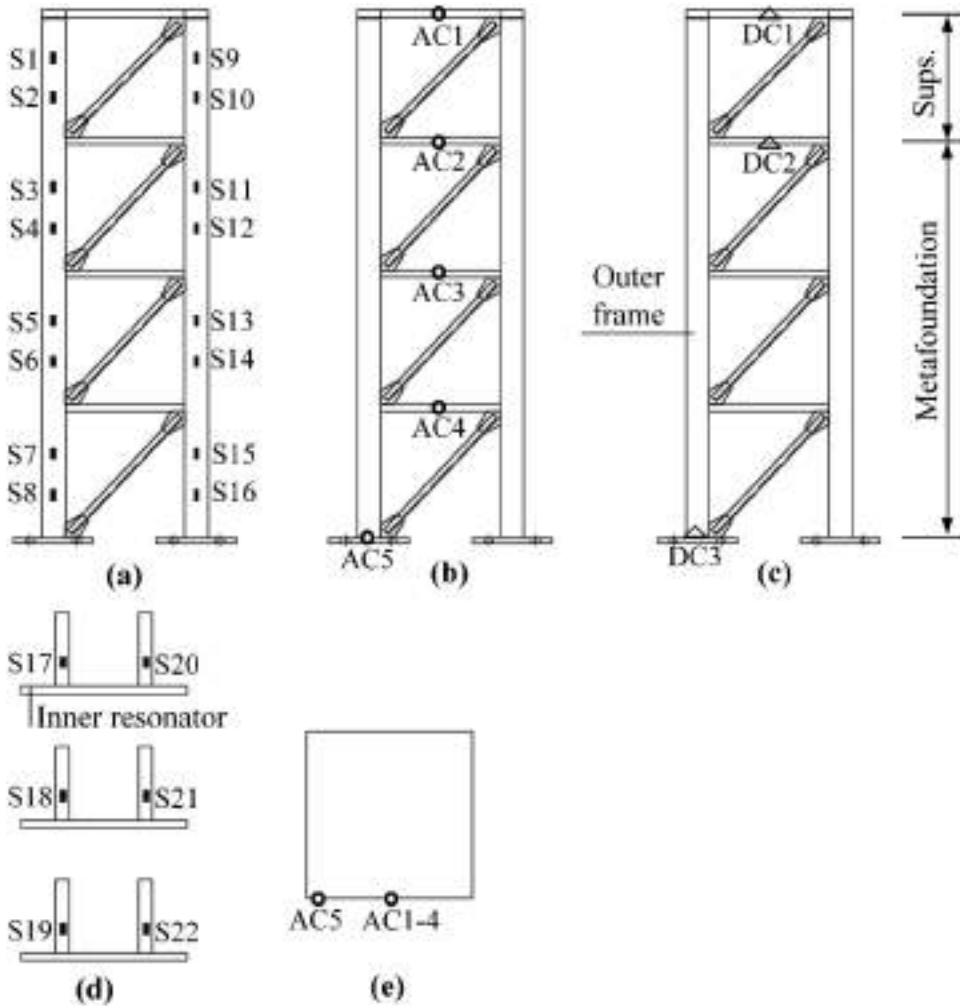


Figure 10. Instrumentation for the controlled superstructure system. The arrangement of (a) strain gauges on columns; (b) accelerometers; (c) displacement meters; (d) strain gauges on the steel strips. (e) Top view of the accelerometer arrangement.

accelerometers: i) accelerometers AS #1–5 were set to investigate the vertical propagation law of seismic waves; ii) accelerometers AS #2, #6, and #8 or iii) AS #5, #7, and #9 to validate the boundary effect.

3.5. Experimental Program

With regard to seismic input, eight accelerograms in total were selected from FEMA P695 far-field set based on numerical results provided by the simplified models. Some information on those accelerograms is provided in Table 2. A summary of the experimental sequence is given in Table 3. The test was conducted in two phases. Phase #1 is the free-field test to study the dynamic properties of the soil-box system, labeled with “FF” in Table 3. In Phase #1, Acc #1–#3 were tested. Phase #2 is the soil-structure interaction test, labeled with “SSI” in Table 3. Five excitation intensities with peak ground accelerations (PGA) ranging from 0.07 g to 0.7 g were included. In the case of 0.07 g PGA, all the eight selected

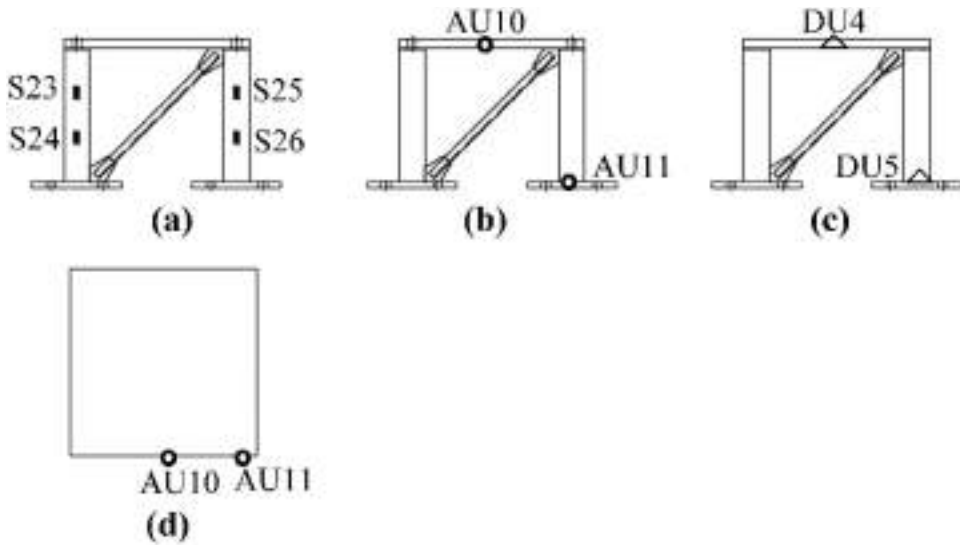


Figure 11. Instrumentation for the uncontrolled superstructure system. The arrangement of the (a) strain gauges on columns; (b) accelerometers; (c) displacement meters. (d) Top view of the accelerometer arrangement.

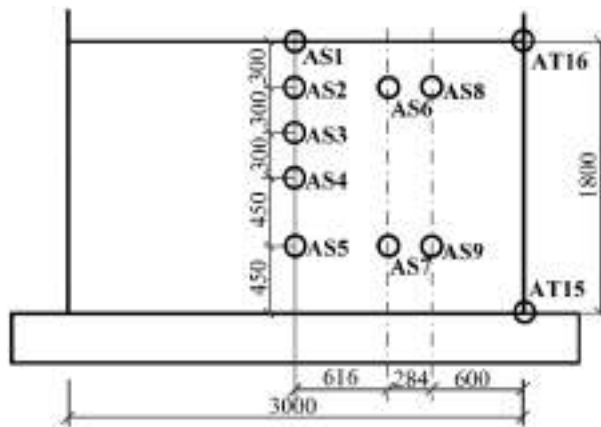


Figure 12. Instrumentation of the soil layer.

accelerograms were tested to provide data at the elastic stage to validate the simplified model in Section 2. For the other four levels of PGA, accelerograms Acc #1–4 were tested. Accelerogram Acc #1 was tested two times at each level to investigate if the soil properties were stable. For simplicity, tests SSI #2, 12, 18, 24, and 30 are grouped as Case #1, while tests SSI #10, 16, 22, 28, and 34 are grouped as Case #2. Before and after each intensity level, a small-amplitude white noise (WN) was applied to determine any change in the system’s dynamic characteristics.

4. Test Result and Discussion

The outcomes of typical tests of the experimental program are discussed hereafter. The primary aims include i) validating the simplified approach in Section 2, and ii) investigating the seismic mitigation performance of metafoundations with SSI.

Table 2. Selected ground motion records.

Number of accelerogram	ID	Time step (s)	Scaled time step (s)	Total time (s)
Acc #1	RSN1148_KOCAELI_ARE000	0.005	0.0025	12.250
Acc #2	RSN767_LOMAP_G03000	0.005	0.0025	20.000
Acc #3	RSN960_NORTHR_LOS270	0.010	0.0050	10.000
Acc #4	RSN1111_KOBE_NIS090	0.010	0.0050	20.500
Acc #5	RSN1633_MANJIL_ABBAR	0.020	0.0100	26.800
Acc #6	RSN68_SFERN_PEL090	0.010	0.0050	39.725
Acc #7	RSN1116_KOBE_SHI000	0.010	0.0050	20.500
Acc #8	RSN829_CAPEMEND_RIO270	0.020	0.0100	18.000

4.1. Free-Field Test Results

The fundamental frequency of the soil layer is obtained by performing spectra analysis on the time-history results of sensor AS #1 in both test FF#1 and FF #5. The relevant transfer functions are shown in Fig. 13. It can be concluded that the fundamental frequency is 6.6 Hz, differing from the designed frequency of 8.8 Hz. By assuming a soil density of 700 kg/m^3 , the transfer function of the soil layer can be obtained from the one-dimensional wave propagation theory, which is also displayed in Fig. 13. Both the test and theoretical results agree with each other at the first-order frequency.

4.2. Validation of the Simplified Models

Test results of 0.07 g PGA are employed to validate the capability of the simplified model in Section 2 to model the system response at the elastic stage. The input parameters of the simplified models can be identified from the test results in the frequency domain based on transfer functions (TFs). Then the simplified model results and test results are compared in both the frequency and time domains.

Table 3. Shaking table test program.

Test program	Input Wave form	PGA (g)
Phase #1:	Free field test	
FF #1	white noise	0.07
FF #2-#4	Acc #1-#3	0.07
FF #5	white noise	0.07
Phase #2:	Soil-structure interaction test	
SSI #1	white noise	0.07
SSI #2	Acc #1	0.07
SSI #3-#9	Acc #2-#8	0.07
SSI #10	Acc #1	0.07
SSI #11	white noise	0.07
SSI #12	Acc #1	0.1
SSI #13-#15	Acc #2-#4	0.1
SSI #16	Acc #1	0.1
SSI #17	white noise	0.07
SSI #18	Acc #1	0.2
SSI #19-#21	Acc #2-#4	0.2
SSI #22	Acc #1	0.2
SSI #23	white noise	0.07
SSI #24	Acc #1	0.4
SSI #25-#27	Acc #2-#4	0.4
SSI #28	Acc #1	0.4
SSI #29	white noise	0.07
SSI #30	Acc #1	0.7
SSI #31-#33	Acc #2-#4	0.7
SSI #34	Acc #1	0.7
SSI #35	white noise	0.07

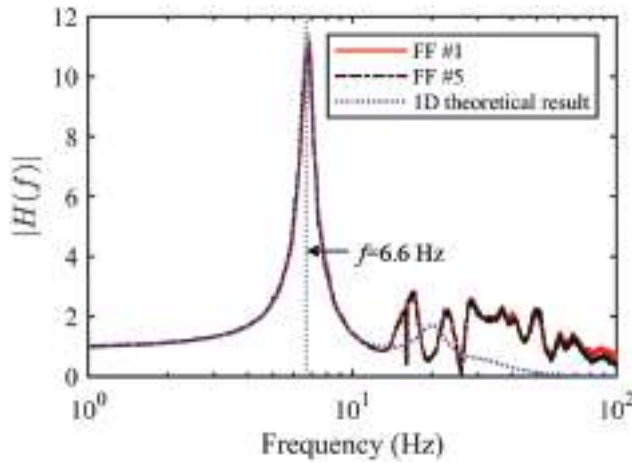


Figure 13. Comparison of the transfer functions of soil layer from records of AS#1 relevant to tests FF#1 and FF#5 and that of the one-dimensional theoretical results.

To eliminate the influence of the frequency content of seismic records, the average TF modulus of the eight tests with PGA equal to 0.07 g was adopted for system parameter identification; then, the transfer function moduli of the simplified model and test results were compared. For the controlled system, in Fig. 14, the simplified model result (thick red line) meets the average test results (thick black line) quite well, which indicates that the simplified model can capture the primary dynamic characteristics of the controlled system. The comparison results for the uncontrolled system are displayed in Fig. 15. Similarly, the numerical model reflects the main frequency of the uncontrolled system well, even though the frequency contents in the frequency region from around 16 Hz to 23 Hz are quite different.

With regard to the acceleration time-history responses, Fig. 16 compares the test results and simplified model results of acceleration response at the top of the controlled superstructure when it was subjected to Acc #5. The comparison relevant to the uncontrolled superstructure is shown in Fig. 17. The peak response ratios of the simplified model results in the test results of the controlled and uncontrolled superstructures are 0.89 and 1.13, respectively. The peak acceleration response of the numerical and test results of all the eight tested accelerograms are summarized in Table 4 and vividly

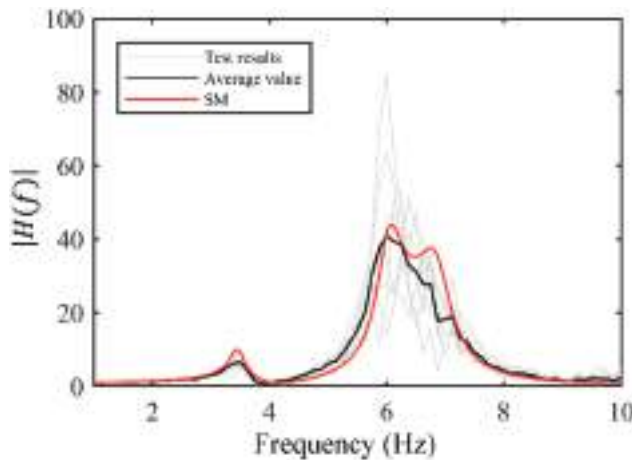


Figure 14. Transfer function moduli $|H_{con}|$ of test results at 0.07g level (light grey lines), their average value (thick black line), and the simplified model (SM) results (thick red line).

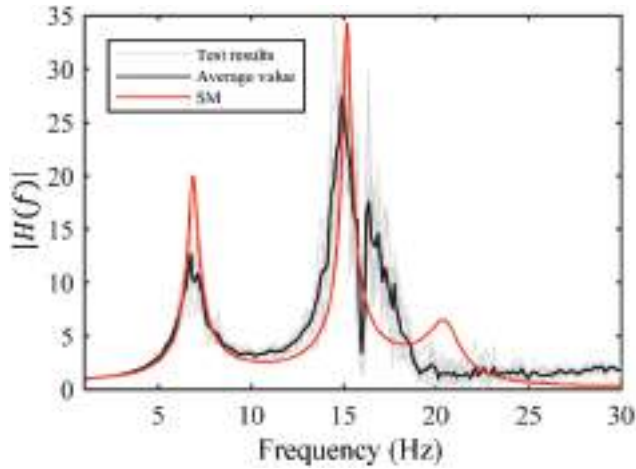


Figure 15. Transfer function moduli $|H_{unc}|$ of test results (light grey lines) at 0.07g level, their average value (thick dark line), and the relevant simplified model (SM) results (thick red line).

illustrated in Fig. 18. The average deviations of the controlled and uncontrolled systems are 18% and 17%, respectively. The maximum deviation is 29%. These results indicate that numerical predictions agree well with the experimental results. Therefore, based on the results in the frequency domain (see Figs. 14 and 15), and time domain (see Figs. 16, 17 and Table 4), the simplified model proposed in Section 2 can capture the main characteristics of the SSI system.

4.3. Vibration Mitigation Performance Evaluation

The vibration mitigation effects can be measured by the peak response ratio of the controlled and uncontrolled superstructure, as indicated here,

$$PI = \max(a^{con}) / \max(a^{unc}) \tag{19}$$

In Eq. (18), $\max(a^{con})$ and $\max(a^{unc})$ are the maximum absolute acceleration response of the controlled and uncontrolled superstructure, which can be obtained from test results of accelerometers AC #1 and AU #10, respectively.

Figure 19 depicts the variation of mitigation effects of four accelerograms as a function of input PGA. Several conclusions can be drawn from the results relevant to the accelerogram Acc #1. As mentioned above and to check the stability of soil properties, Acc #1 was tested two times at each intensity level. As shown in Fig. 19, the performance indices of Case #1 -tests at the

Table 4. Peak value ratios of numerical results to test results.

Accelerogram	The controlled superstructure			The uncontrolled superstructure		
	Numerical result (g)	Test result (g)	Numerical result/test result	Numerical result (g)	Test result (g)	Numerical result/test result
Acc #1	0.26	0.31	0.85	0.31	0.43	0.71
Acc #2	0.51	0.63	0.81	0.45	0.55	0.80
Acc #3	0.57	0.55	1.03	0.33	0.37	0.90
Acc #4	0.52	0.71	0.74	0.42	0.51	0.84
Acc #5	0.54	0.61	0.89	0.35	0.31	1.13
Acc #6	0.64	0.82	0.78	0.58	0.58	1.01
Acc #7	0.44	0.56	0.79	0.32	0.40	0.80
Acc #8	0.69	0.92	0.75	0.31	0.41	0.76

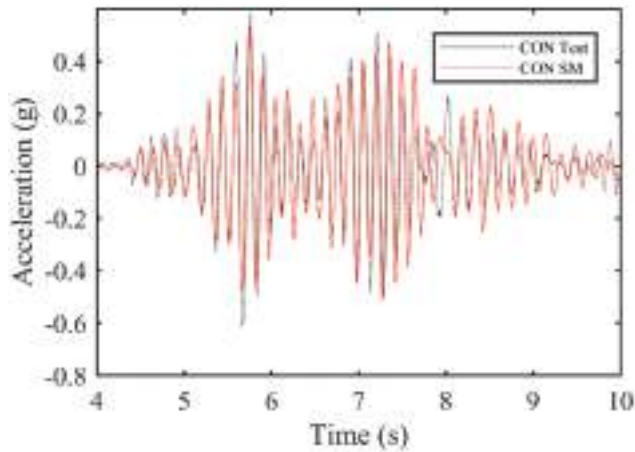


Figure 16. Test results and simplified model results of acceleration responses at the top of the controlled superstructure for Acc #5, with $PGA=0.07g$.

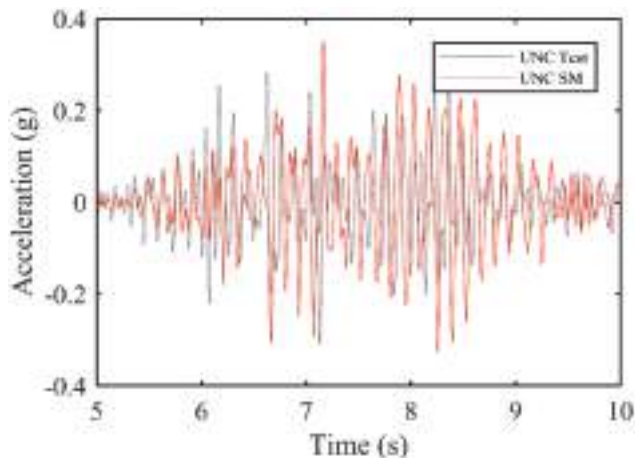


Figure 17. Test results and simplified model results of acceleration responses at the top of the uncontrolled superstructure for Acc #6, with $PGA=0.07g$.

beginning of each level- and Case #2 -tests at the end of each level- at the same input PGA are very close, which indicates that the soil properties are stable at each stage. All the performance indices are less than one, which proves the seismic mitigation efficiency of the designed metafoundation. Moreover, the peak acceleration response of the controlled system is, on average, 31% smaller than that of the uncontrolled system. Furthermore, when the superstructure is subjected to excitation Acc#1, one can observe that the input PGA has little influence on the mitigation effect.

Apart from Acc #1, the vibration mitigation effects of the other three accelerograms are improved as PGA values are increased. In the case of Acc #2, when $PGA \leq 0.1g$, the peak response of the controlled superstructure is more significant than that of the uncontrolled superstructure; when $PGA > 0.1g$, the performance indices indicate that the metafoundation can mitigate the response of the superstructure to some extent. More specifically, the average mitigation effect of the three cases when input PGA is larger than 0.1 g is around 27%. In the case of Acc #3, a 12% mitigation effect is achieved when PGA approaches 0.7 g. For Acc #4, in the tested PGA

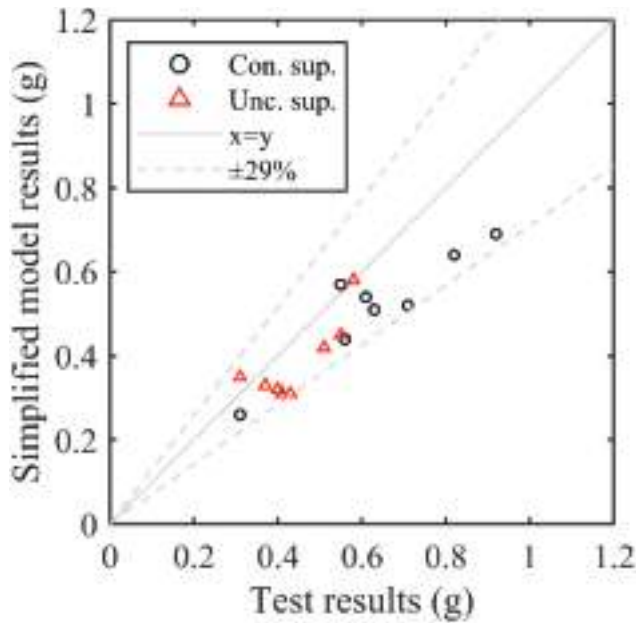


Figure 18. Peak acceleration response of test results versus simplified model results. ‘Con. sup.’ and ‘Unc. sup.’ stand for ‘Controlled superstructure’ and ‘Uncontrolled superstructure,’ respectively.

range, the response of the controlled superstructure is more significant than that of the uncontrolled superstructure. However, the performance is improved when the PGA is increased.

By comparing performance at different input PGA levels, it can be found that the metafoundation achieves better mitigation performance at larger input PGA levels. More specifically, at 0.7 g PGA, the metafoundation is efficient with three out of four accelerograms, achieving a 28% average mitigation effect. However, at 0.1 g PGA, the metafoundation is efficient only with one accelerogram. Figure 20a

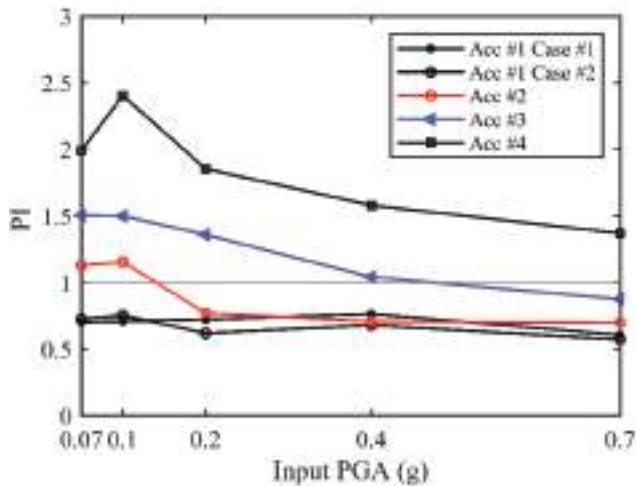


Figure 19. Variation of mitigation effects versus input PGA.

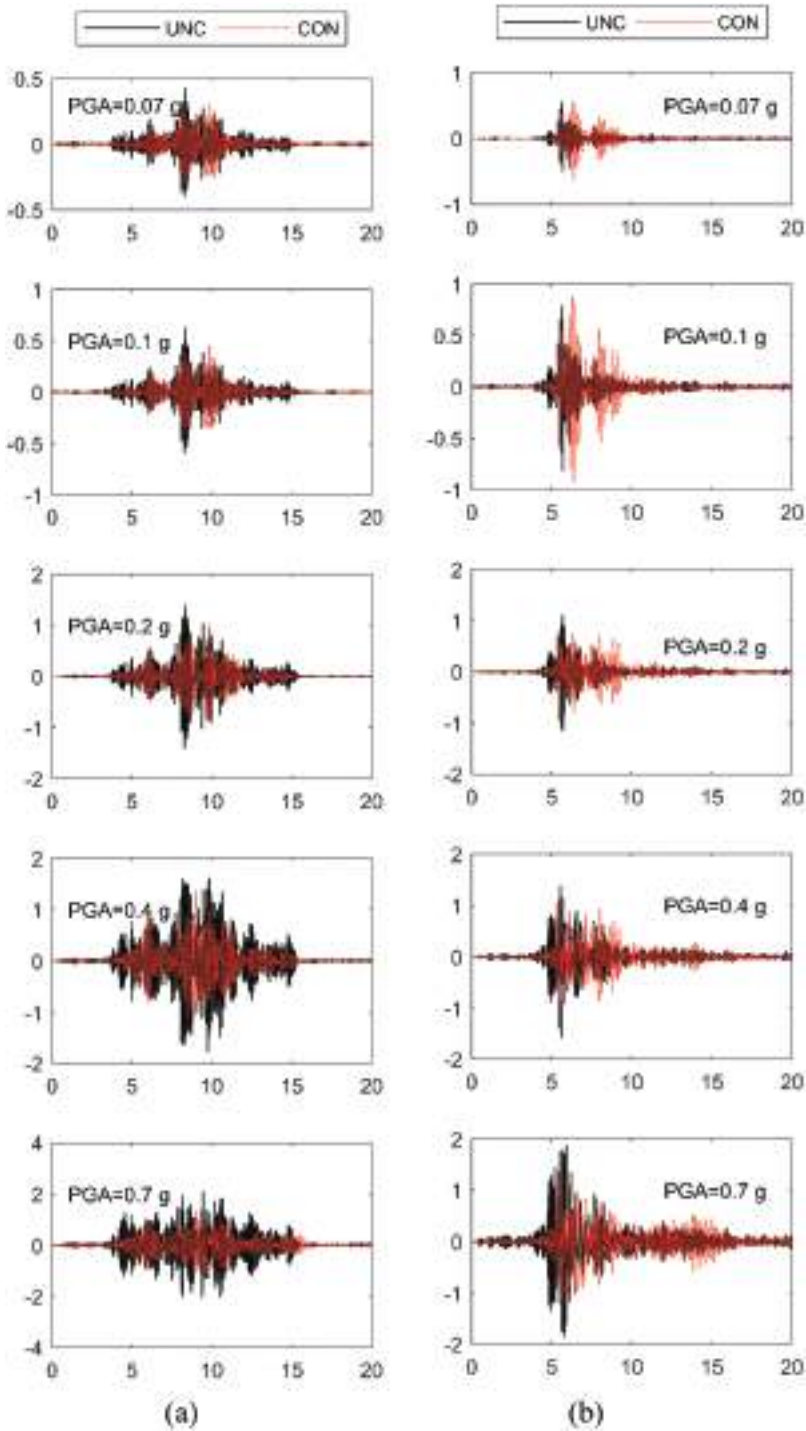


Figure 20. Time history response of both the controlled and uncontrolled superstructure at different input PGA levels subjected to: (a) Acc#1 and (b) Acc#2.

displays comparisons among the acceleration time–history curves of the controlled and uncontrolled superstructure subjected to Acc #1 at different intensities, which directly highlights the effectiveness of the metafoundation on the mitigation effect of the seismic response. The results relevant to Acc#2 are shown in Fig. 20b. At $\text{PGA} \leq 0.1 \text{ g}$, the peak response of the controlled superstructure is more significant than that of the uncontrolled superstructure. Nonetheless, when $\text{PGA} > 0.1 \text{ g}$, the peak response of the controlled superstructure is smaller than that of the uncontrolled superstructure.

4.4. Performance Influence of the Frequencies of the Input Motions

Time-frequency representations based on the Short-Time Fourier Transform (STFT) are employed to visualize the frequencies of each accelerogram and explain the different mitigation effects achieved between Acc #1 and the other three accelerograms. Overall, the STFT corresponds to the computation of a signal's Power Spectral Density (PSD) by using a moving window of data, allowing the construction of a time-frequency representation (Hernández et al. 2021).

Figure 21 displays the spectrograms of the four accelerograms. The energy of Acc #1 is concentrated on the frequency range of 11–15 Hz, while that of the other three mainly spreads in the frequency range below 10 Hz with a high concentration below 5 Hz. The accelerations near the soil layer surface recorded by sensor AS #1 can reflect both the frequency characteristics of the input accelerogram and the soil layer. The spectrograms of these accelerations are exhibited in Fig. 22. Each column of the figure corresponds to the results of one accelerogram, and each row corresponds to one input PGA. The input PGA increases from 0.1 g to 0.7 g from top to bottom. These figures indicate that, after interacting with the soil layer, the frequency components of Acc #1 in the range higher than 10 Hz are still prominent compared with the other three accelerograms. The eigenfrequency of the tested uncontrolled superstructure is around 14.75 Hz, and that of the controlled superstructure is 6.25 Hz. Hence, compared with the other three accelerograms, Acc #1 is more comparatively critical to the uncontrolled superstructure. Response amplification factors of the superstructures relative to the response of the soil layer surface are employed for quantitative comparison. Response amplification factors are defined as the peak response ratio of the controlled (uncontrolled) superstructure to the soil layer surface. As displayed in Fig. 23a, in the case of the uncontrolled superstructure, three amplification factors of Acc #1 are significantly larger than those of the other three accelerograms. On the contrary, the amplification factors of the controlled superstructure in the case of Acc #1 are not more significant than in any other cases.

4.5. Performance Influence of SSI

The interesting phenomenon in Subsection 4.3 that the metafoundation exhibits better mitigation effects at larger PGA levels is explained thoroughly in this subsection.

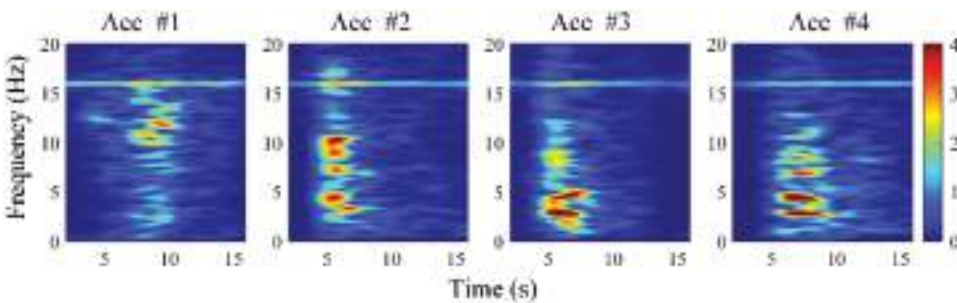


Figure 21. Spectrograms of Acc#1-#4.

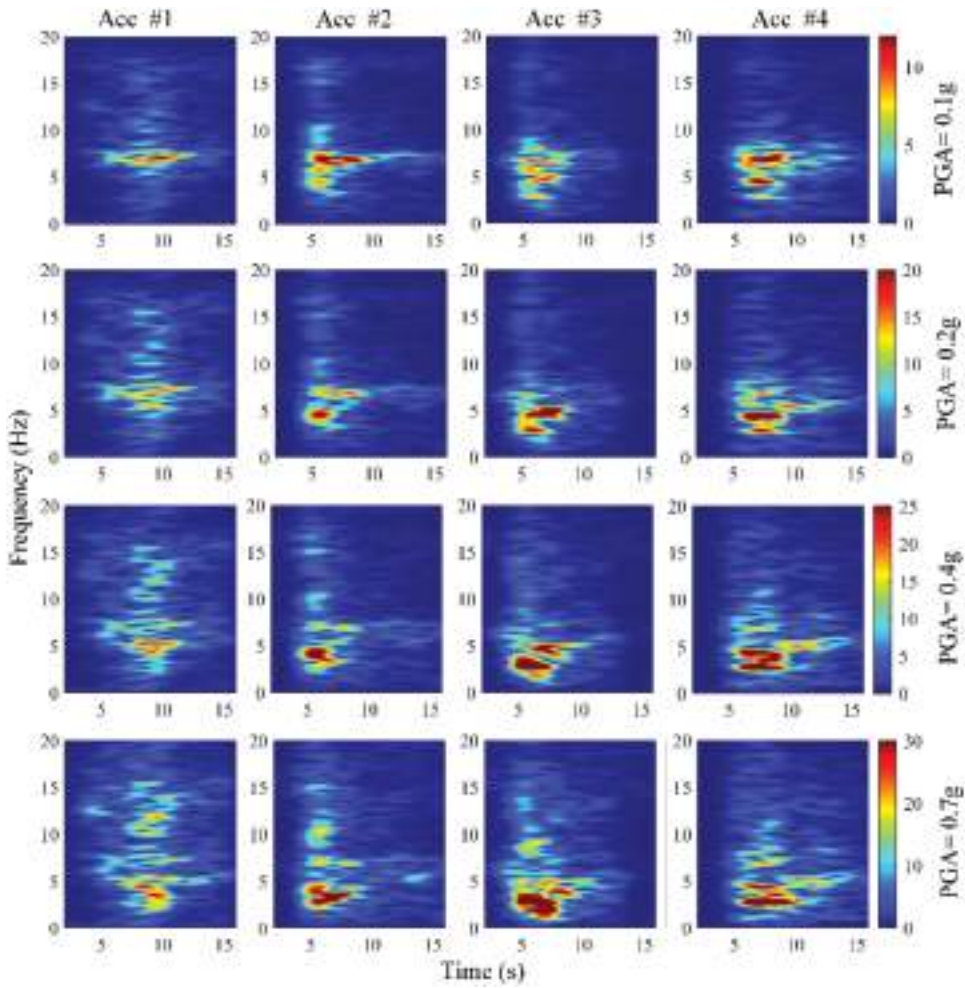


Figure 22. Spectrograms of accelerations near the soil layer surface. Each column corresponds to the results of one accelerogram and each row corresponds to one input PGA.

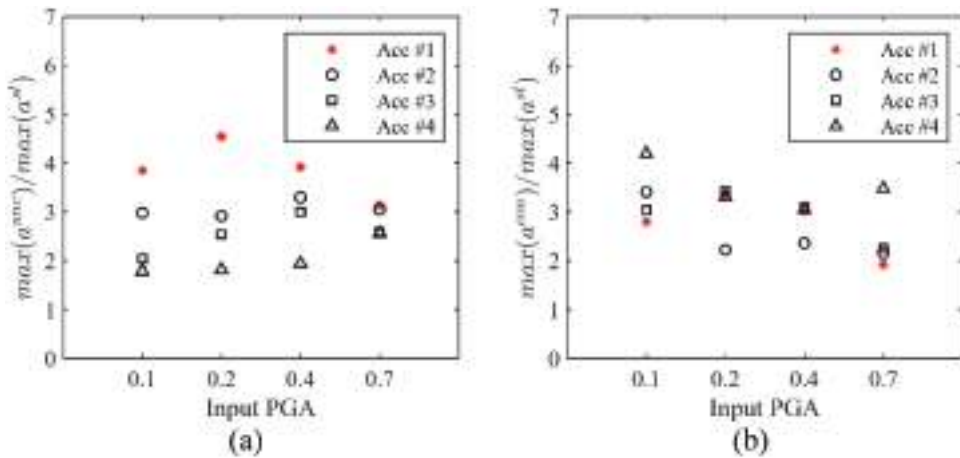


Figure 23. Response amplification factors of the superstructures relative to the response of the soil layer surface: (a) results of the uncontrolled superstructure and (b) those of the controlled one. 'max(a^{con})', 'max(a^{uncon})' and 'max(a^s)' represent the peak acceleration response of the controlled superstructure, uncontrolled superstructure and soil layer surface, respectively.

4.5.1. Interpretation with Time-Frequency Representations

Hernandez et al. proposed a time-frequency method, namely, the Short Time Transfer Function (STTF) method, based on the transfer function's numerical computation by short-time windows of data (Hernández et al. 2021). The computation of the STTF was executed by using a Hanning window that multiplies the input and output signals previous to the computation of its spectral ratio. The STTF is similar to a spectrogram, but it describes the transfer function between one input and one output rather than the output signal's power spectral density only (i.e. a spectrogram).

In this subsection, the STTF method is applied to track the time evolution of eigenfrequencies of the systems and subsystems, including the controlled/uncontrolled superstructure and soil layer. More specific, STTFs were calculated for evaluating the properties of the following systems/subsystems:

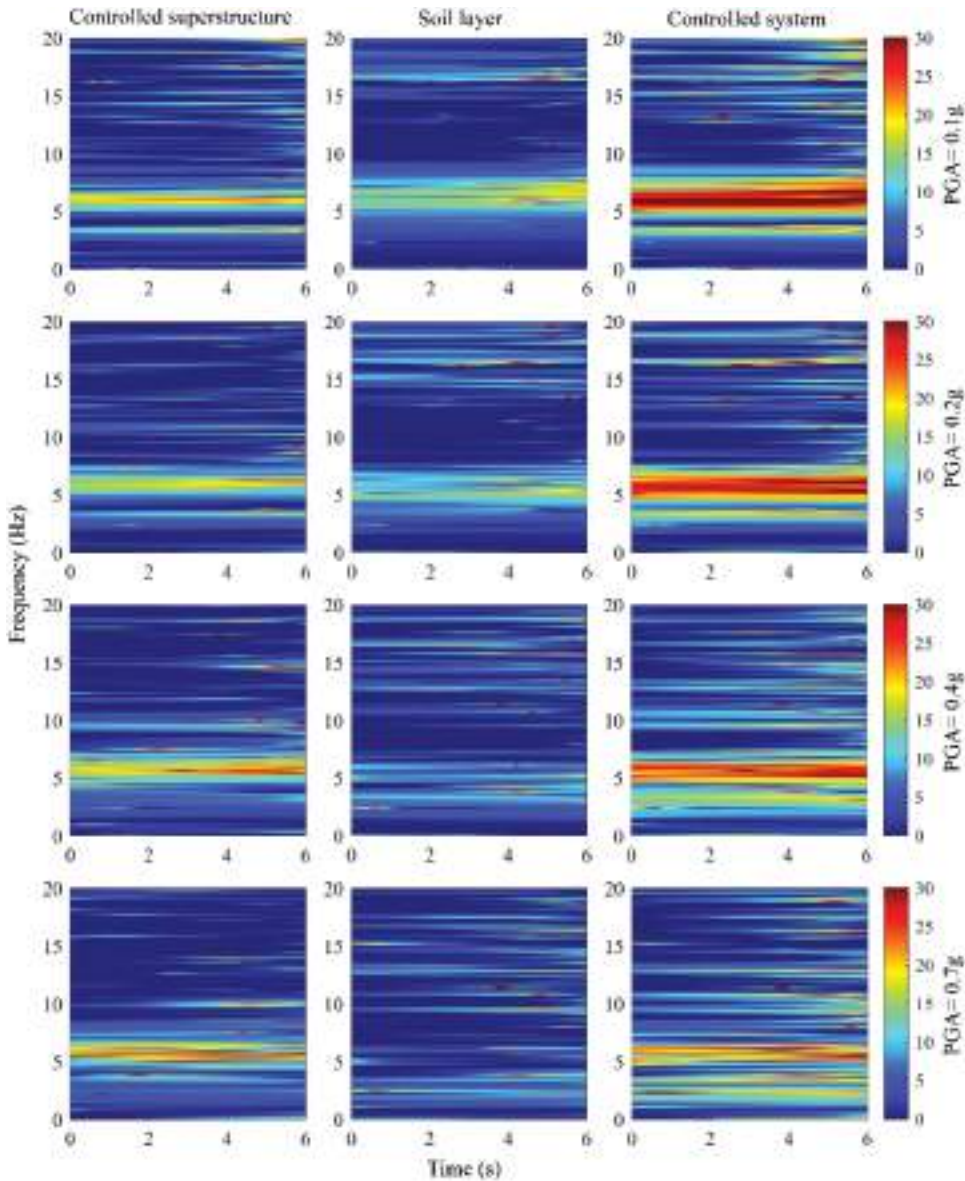


Figure 24. Short Time Transfer Function of the controlled superstructure, the soil layer and the controlled system in the case of Acc #3.

- the controlled/uncontrolled superstructure; computed by the accelerogram at the top of the superstructure and that at the base plate;
- the soil layer; computed by the accelerogram at the top of the soil layer and the shaking table input.
- the controlled/uncontrolled system; computed by the accelerogram at the top of the superstructure and the shaking table input.

The STTFs of the controlled superstructure are displayed in the first column of Fig. 24. As input PGA increases from 0.1 g to 0.7 g, the main eigenfrequency of the superstructure remains around 5.87 Hz. However, the eigenfrequency of the resonators, which is 3.37 Hz at 0.1 g PGA, became obscure from

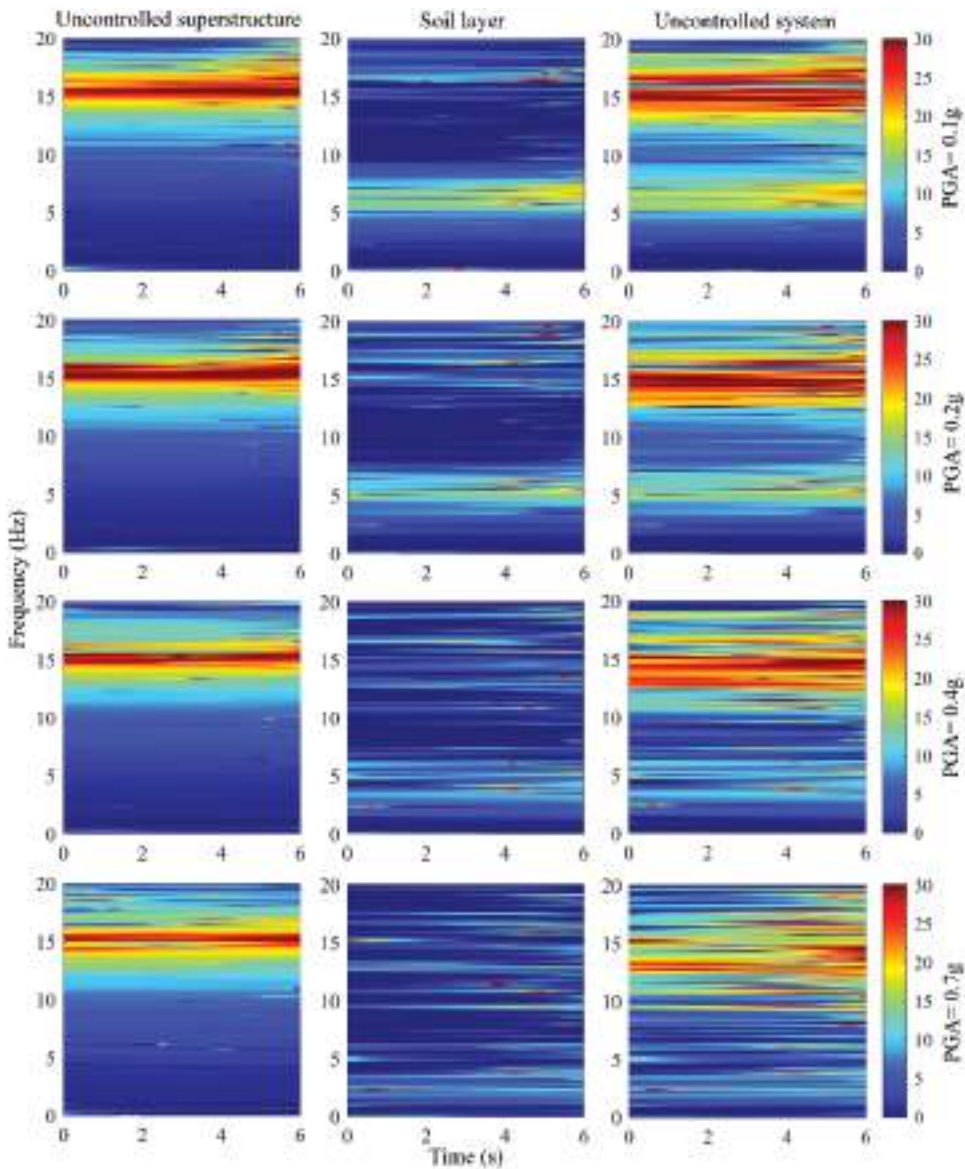


Figure 25. Short Time Transfer Function of the uncontrolled superstructure, the soil layer and the uncontrolled system in the case of Acc #3.

0.4 g PGA. The second column of Fig. 24 presents the STTFs of the soil layer. As the PGA increases, the eigenfrequency of the soil layer moves from 6.60 Hz to a lower frequency of around 2.50 Hz. The energy distributions are less concentrated. The third column displays the results of the controlled system. Due to resonance between the controlled superstructure and the soil layer, the energy concentrates mainly around 6.00 Hz. As the input PGA increases and the eigenfrequency of the soil layer shifts to the lower frequency range, the energy gradually spreads in a broader and lower frequency range. Figure 25 displays the results of the uncontrolled system and its subsystems for comparison. From the figures in the first column of Fig. 25, it can be concluded that the eigenfrequency of the uncontrolled superstructure remains around 15.00 Hz during the whole testing process. The eigenfrequency of the uncontrolled superstructure is far away from that of the soil layer. Hence, no obvious resonance is observed in the uncontrolled system.

4.5.2. Interpretation Based on Equivalent Linear Properties

Even though the simplified models proposed in Section 2 are valid in a linear elastic regime, the simplified model contributes to understanding test results by using equivalent linear properties. In this respect, the transfer function moduli of the controlled system from both the test results and the simplified model subjected to accelerogram Acc #3 -PGA of 0.1 g- are displayed in Fig. 26a. One can deduce that the fundamental frequency of the soil layer (6.62 Hz) and that of the controlled superstructure (5.87 Hz) are very close, and the two peak frequencies reflect this. Therefore, the resonance phenomenon described above for PGA = 0.07 g is observed again.

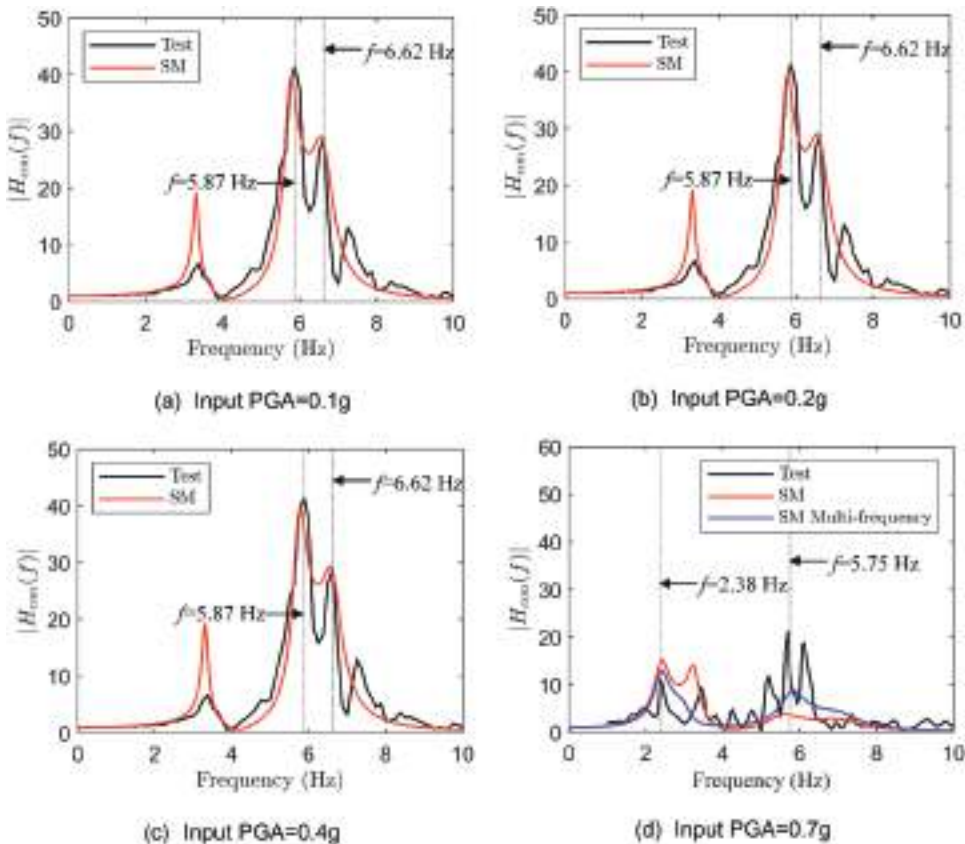


Figure 26. Moduli of transfer functions of the controlled system $|H_{con}|$ when subjected to Acc#3.

Table 5. Input parameters of the simplified model to simulate test results of the controlled superstructure subjected to Acc #3.

Input PGA (g)	ξ_2	ξ^i	ξ_f	ξ_{soil}	f_{soil}	f_{sup}	wd	k_2/k_{20}
0.1	0.04	0.02	0.02	0.04	6.625	5.875	2048	1.00
0.2	0.08	0.02	0.02	0.04	5.250	5.875	2048	1.00
0.4	0.08	0.02	0.02	0.06	5.125	5.750	2048	1.00
0.7	0.08	0.02	0.02	0.08	2.375	5.750	2048	1.00

Notes: ξ_2 —The damping ratio of inner resonators.
 ξ^i - The damping ratio of the superstructure
 ξ_f - The damping ratio of the outer frame
 ξ_{soil} - The damping ratio of the soil layer
 f_{soil} - The dominant frequency of the soil layer
 f_{sup} - The dominant frequency of the superstructure
 wd- Width of hamming window when calculating transfer function
 k_{20} - Initial stiffness of inner resonators
 k_2 - Stiffness of inner resonators adopted in the simplified model

When the input PGA is increased to 0.2 g, the eigenfrequency of the superstructure remains the same, while that of the soil layer shifts from 6.62 Hz to 5.25 Hz, as indicated in Fig. 26b. The maximum amplitude also decreases. These phenomena suggest that when the input PGA has increased to 0.2 g, the soil damping ratio increases, and its elastic modulus decreases.

Figure 26c shows the results in the case of 0.4 g PGA. Obvious frequency shifts are not observed when compared with the results in the case of 0.2 g PGA. However, the energy in the low-frequency band spreads over a broader frequency range. The transfer function of the simplified model with multi-frequency resonators- denoted as H_{con} SM Multi-frequency in Fig. 26c- agrees with the test result better than that of the simplified model with single-frequency resonators- denoted as “ H_{con} SM” in Fig. 26c-. Hence, at the seismic level of 0.4 g, the frequencies of the three inner resonators vary due to inelasticity. Other studies have explored the benefits of metamaterials with multi-frequency resonators (Bursi, Basone, and Wenzel 2021; Colombi et al. 2016; Krödel, Thomé, and Daraió 2015; Meng et al. 2020). When the input PGA is increased to 0.7 g, the soil eigenfrequency shifts to 2.38 Hz, and the stiffnesses of the inner resonators decay, as shown in Fig. 26d.

The equivalent linear parameters of the simplified models are listed in Table 5. As the input PGA is increased from 0.1 g to 0.7 g, the damping ratio of the soil layer ξ_{soil} and the inner resonators ξ_2 increase. The eigenfrequency of the soil f_{soil} shifts from 6.62 Hz to 2.37 Hz but the eigenfrequency of the superstructure f_{sup} remains almost the same.

Similar phenomena are also observed in the test results with Acc #2 and Acc #4. The results of Acc #2 in the case of 0.1 g PGA and 0.7 g PGA are displayed in Fig. 27a,b, respectively. The comparison of these figures highlights the aforementioned trend.

Thus, we can summarize the reasons why the metafoundation achieves better performance at larger input PGA levels as follows: i) the counteracting effect of the resonance due to the increase in soil damping ratio and the dominant frequency shift of soil layer; ii) the positive contribution of multi-frequency resonators to vibration mitigation.

5. Conclusions

This paper presented the results of an experimental investigation on the seismic mitigation performance of metafoundations with soil-structure interaction. Both the controlled and uncontrolled systems were embedded in a dry bed of sand-sawdust mixture and within a flexible soil container. The experimental system was subjected to various ground motions at multiple PGA levels. Meanwhile, a simplified mechanical model was proposed to estimate the elastic response of the controlled system. The good correlations between analytical and experimental results confirm the ability of the model to capture global responses at the elastic stage in both the time and frequency domain.

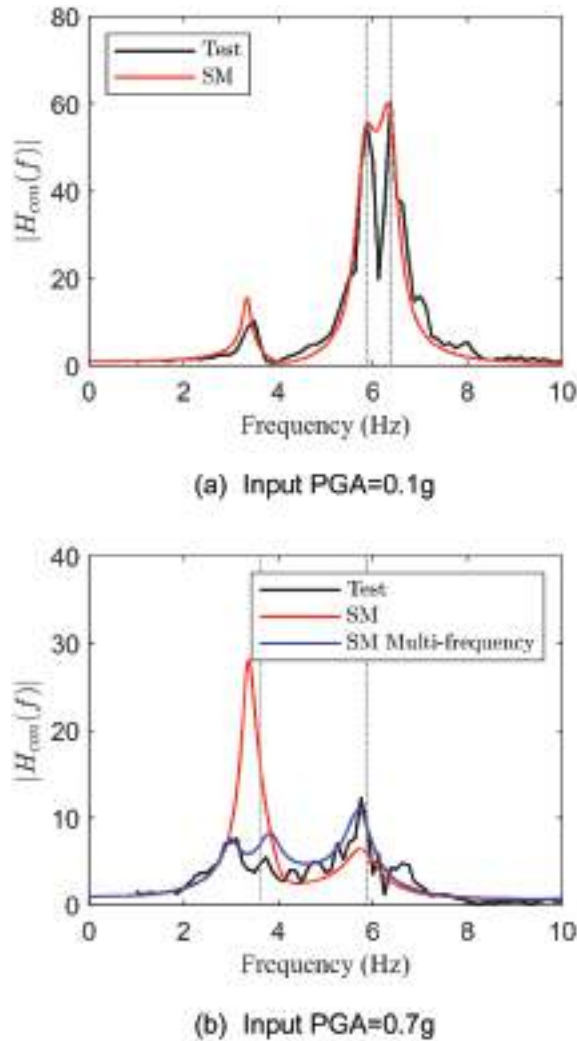


Figure 27. Moduli of transfer functions of the controlled system $|H_{con}|$ when subjected to Acc#2.

The test results revealed that metafoundation performance strongly depended on the degree of coupling among the frequencies of the soil layer, the structural system, and the input motion. Time-frequency representation methods and the validated simplified model with equivalent linear parameters were employed to provide a thorough explanation. Among the four tested accelerograms, the metafoundation efficiently mitigated the superstructure's response subjected to Acc #1 at all the tested PGA levels. The peak acceleration response of the controlled system was, on average, 31% smaller than that of the uncontrolled system. Spectrogram results indicated that the energy of Acc #1 is mainly concentrated in the high-frequency range, which is more critical to the uncontrolled structure.

With respect to performance at different input PGA levels, the metafoundation achieved better mitigation performance at large input PGA levels compared with the performance at small input PGA levels. More specifically, at 0.7 g PGA, the metafoundation was efficient with three out of four accelerograms, achieving a 28% average mitigation effect. However, at 0.1 g PGA, the metafoundation was efficient only with one accelerogram. Based on the analysis results of time-frequency representations and simplified models, it can be concluded that favorable effects occurred due to the increase in soil damping ratio and soil layer dominant frequency shift; moreover, due to inelasticity, the frequency

of inner resonators changed from single-frequency into multi-frequency, which also significantly contributed to improving mitigation effects.

The experimental program documented in this paper provided unique data on seismic mitigation performance of metafoundation with SSI considered. The satisfactory performance of the metafoundation at large input PGA confirmed their efficiency in mitigating structure vibration. However, its performance highly depends on the degree of coupling among the frequencies of the soil layer, the structural system, and the input motion, which should be carefully considered in the design of a metafoundation. The validated simplified model, which can predict the response with acceptable accuracy, can be used for preliminary calculation. Conditions with lateral SSI and multiple soil layers would be considered to move into wider practice for further studies. Last but not least, practical treatment should be developed to allow the free deformation of the metafoundation buried in the soil.

Acknowledgments

This work received support from the National Natural Science Foundation of China (No. 51778488) for the first two authors and the Italian Ministry of Education, University and Research (MIUR) in the frame of the ‘Departments of Excellence’ (grant L 232/2016) for the third author. Moreover, the useful discussion with Prof. Francisco Hernandez—Department of Civil Engineering, University of Chile—about calculation of Short-Time Transfer Function is acknowledged.

Disclosure Statement

No potential conflict of interest was reported by the authors.

Funding

The work was supported by the National Natural Science Foundation of China [No. 51778488]; the Italian Ministry of Education, University and Research (MIUR) in the frame of the ‘Departments of Excellence’ [grant L 232/2016].

ORCID

Heng Li  <http://orcid.org/0000-0002-3187-9041>

References

- Achaoui, Y., B. Ungureanu, S. Enoch, S. Brûlé, and S. Guenneau. 2015. Seismic waves damping with arrays of inertial resonators. *Extreme Mechanics Letters* 8:30–37. doi:10.1016/j.eml.2016.02.004.
- Anastasopoulos, I., M. Loli, T. Georgarakos, and V. Drosos. 2013. Shaking table testing of rocking—isolated bridge pier on sand. *Journal of Earthquake Engineering* 17 (1):1–32. doi:10.1080/13632469.2012.705225.
- Basone, F., M. Wenzel, O. S. Bursi, and M. Fossetti. 2019. Finite locally resonant Metafoundations for the seismic protection of fuel storage tanks. *Earthquake Engineering & Structural Dynamics* 48 (2):232–52. doi:10.1002/eqe.3134.
- Brûlé, S., S. Enoch, and S. Guenneau. 2020. Emergence of seismic metamaterials: Current state and future perspectives. *Physics Letters* 384 (1):126034. doi:10.1016/j.physleta.2019.126034.
- Brûlé, S., E. Javelaud, S. Enoch, and S. Guenneau. 2014. Experiments on seismic metamaterials: Molding surface waves. *Physical Review Letters* 112 (13):133901. doi:10.1103/PhysRevLett.112.133901.
- Bursi, O. S., F. Basone, and M. Wenzel. 2021. Stochastic analysis of locally resonant linear and hysteretic metamaterials for seismic isolation of process equipment. *Journal of Sound and Vibration* 510:116263. doi:10.1016/j.jsv.2021.116263.
- Casablanca, O., G. Ventura, F. Garesci, B. Azzeroni, B. Chiaia, M. Chiappini, and G. Finocchio. 2018. Seismic isolation of buildings using composite foundations based on metamaterials. *Journal of Applied Physics* 123 (17):174903. doi:10.1063/1.5018005.
- Chen, Z., W. Chen, Y. Li, and Y. Yuan. 2016. Shaking table test of a multi-story subway station under pulse-like ground motions. *Soil Dynamics and Earthquake Engineering* 82:111–22. doi:10.1016/j.soildyn.2015.12.002.
- Cheng, Z., Z. Shi, A. Palermo, H. Xiang, W. Guo, and A. Marzani. 2020. Seismic vibrations attenuation via damped layered periodic foundations. *Engineering Structures* 211:110427. doi:10.1016/j.engstruct.2020.110427.
- Colombi, A., D. Colquitt, P. Roux, S. Guenneau, and R. V. Craster. 2016. A seismic metamaterial: The resonant metawedge. *Scientific reports* 6 (1):6. doi:10.1038/srep27717.

- Colombi, A., P. Roux, S. Guenneau, P. Gueguen, and R. V. Craster. 2016. Forests as a natural seismic metamaterial: Rayleigh wave bandgaps induced by local resonances. *Scientific reports* 6 (1):19238. doi:10.1038/srep19238.
- Colombi, A., R. Zaccherini, G. Aguzzi, A. Palermo, and E. Chatzi. 2020. Mitigation of seismic waves: Metabarriers and metafoundations bench tested. *Journal of Sound and Vibration* 485:115537. doi:10.1016/j.jsv.2020.115537.
- Durante, M. G., L. Di Sarno, G. Mylonakis, C. A. Taylor, and A. L. Simonelli. 2016. Soil–pile–structure interaction: Experimental outcomes from shaking table tests. *Earthquake Engineering & Structural Dynamics* 45 (7):1041–61. doi:10.1002/eqe.2694.
- Franchini, A., O. S. Bursi, F. Basone, and F. Sun. 2020. Finite locally resonant metafoundations for the protection of slender storage tanks against vertical ground accelerations. *Smart Materials and Structures* 29 (5):055017. doi:10.1088/1361-665X/ab7e1d.
- Geng, Q., S. Zhu, and K. P. Chong. 2018. Issues in design of one-dimensional metamaterials for seismic protection. *Soil Dynamics and Earthquake Engineering* 107:264–78. doi:10.1016/j.soildyn.2018.01.028.
- Hernández, F., P. Díaz, R. Astroza, F. Ochoa-Cornejo, and X. Zhang. 2021. Time variant system identification of superstructures of base-isolated buildings. *Engineering Structures* 246:112697. doi:10.1016/j.engstruct.2021.112697.
- Huang, J., Y. Liu, and Y. Li. 2019. Trees as large-scale natural phononic crystals: Simulation and experimental verification. *International Soil and Water Conservation Research* 7 (2):196–202. doi:10.1016/j.iswcr.2019.03.004.
- Krödel, S., N. Thomé, and C. Daraio. 2015. Wide band-gap seismic metastructures. *Extreme Mechanics Letters* 4:111–17. doi:10.1016/j.eml.2015.05.004.
- Kumar, H., and S. K. Saha. 2021. Effects of soil-structure interaction on seismic response of fixed base and base isolated liquid storage tanks. *Journal of Earthquake Engineering* 26 (12):1–24. doi:10.1080/13632469.2021.1911887.
- La Salandra, V., M. Wenzel, O. S. Bursi, G. Carta, and A. B. Movchan. 2017. Conception of a 3D metamaterial-based foundation for static and seismic protection of fuel storage tanks. *Frontiers in Materials* 4. doi:10.3389/fmats.2017.00030.
- Lim, M. C. W., and J. N. Reddy. 2019. Built-up structural steel sections as seismic metamaterials for surface wave attenuation with low frequency wide bandgap in layered soil medium. *Engineering Structures* 188:440–51. doi:10.1016/j.engstruct.2019.03.046.
- Liu, Y.-F., J.-K. Huang, Y.-G. Li, and Z.-F. Shi. 2019. Trees as large-scale natural metamaterials for low-frequency vibration reduction. *Construction and Building Materials* 199:737–45. doi:10.1016/j.conbuildmat.2018.12.062.
- Liu, X., Y. Wang, and Y. Chen. 2019. Attenuation zones of two-dimensional periodic foundations including the effect of vertical loads. *Applied Sciences* 9 (5):993. doi:10.3390/app9050993.
- Livaoglu, R. 2008. Investigation of seismic behavior of fluid–rectangular tank–soil/foundation systems in frequency domain. *Soil Dynamics and Earthquake Engineering* 28 (2):132–46. doi:10.1016/j.soildyn.2007.05.005.
- Li, P., J. Yang, and Z. Lu. 2018. Shaking table test and theoretical analysis of the pile–soil–structure interaction at a liquefiable site. *The Structural Design of Tall and Special Buildings* 27 (15):e1513. doi:10.1002/tal.1513.
- Lu, X., P. Li Y. Chen, and B. Chen 2004. Shaking table model testing on dynamic soil-structure interaction system. In *Proceedings of the 13th World Conference on Earthquake Engineering*.
- Martakis, P., G. Aguzzi, V. K. Dertimanis, E. N. Chatzi, and A. Colombi. 2021. Nonlinear periodic foundations for seismic protection: Practical design, realistic evaluation and stability considerations. *Soil Dynamics and Earthquake Engineering* 150:106934. doi:10.1016/j.soildyn.2021.106934.
- Meng, H., D. Chronopoulos, A. T. Fabro, W. Elmadih, and I. Maskery. 2020. Rainbow metamaterials for broadband multi-frequency vibration attenuation: Numerical analysis and experimental validation. *Journal of Sound and Vibration* 465:18. doi:10.1016/j.jsv.2019.115005.
- Mu, D., H. Shu, L. Zhao, and S. An. 2020. A review of research on seismic metamaterials. *Advanced Engineering Materials* 22 (4):1901148. doi:10.1002/adem.201901148.
- Palermo, A., S. Krödel, A. Marzani, and C. Daraio. 2016. Engineered metabarrier as shield from seismic surface waves. *Scientific Reports* 6 (1):39356. doi:10.1038/srep39356.
- Palermo, A., M. Vitali, and A. Marzani. 2018. Metabarriers with multi-mass locally resonating units for broad band Rayleigh waves attenuation. *Soil Dynamics and Earthquake Engineering* 113:265–77. doi:10.1016/j.soildyn.2018.05.035.
- Pu, X. B., A. Palermo, Z. Cheng, Z. Shi, and A. Marzani. 2020. Seismic metasurfaces on porous layered media: Surface resonators and fluid-solid interaction effects on the propagation of Rayleigh waves. *International Journal of Engineering Science* 154:154. doi:10.1016/j.ijengsci.2020.103347.
- Pu, X., and Z. Shi. 2018. Surface-wave attenuation by periodic pile barriers in layered soils. *Construction and Building Materials* 180:177–87. doi:10.1016/j.conbuildmat.2018.05.264.
- Pu, X., and Z. Shi. 2020. Broadband surface wave attenuation in periodic trench barriers. *Journal of Sound and Vibration* 468:115130. doi:10.1016/j.jsv.2019.115130.
- Pu, X., Z. Shi, and H. Xiang. 2018. Feasibility of ambient vibration screening by periodic geofoam-filled trenches. *Soil Dynamics and Earthquake Engineering* 104:228–35. doi:10.1016/j.soildyn.2017.10.022.
- Shi, Z. F., and J. K. Huang. 2013. Feasibility of reducing three-dimensional wave energy by introducing periodic foundations. *Soil Dynamics and Earthquake Engineering* 50:204–12. doi:10.1016/j.soildyn.2013.03.009.
- Sun, F., X. Dai, Y. Liu, and L. Xiao. 2021. Seismic mitigation performance of periodic foundations with inertial amplification mechanism considering superstructure–foundation interaction. *Smart Materials and Structures* 30 (2):025018. doi:10.1088/1361-665X/abd58e.

- Sun, F., L. Xiao, and O. S. Bursi. 2019. Optimal design and novel configuration of a locally resonant periodic foundation (LRPF) for seismic protection of fuel storage tanks. *Engineering Structures* 189:147–56. doi:10.1016/j.engstruct.2019.03.072.
- Sun, F., L. Xiao, and O. S. Bursi. 2020. Quantification of seismic mitigation performance of periodic foundations with soil-structure interaction. *Soil Dynamics and Earthquake Engineering* 132:106089. doi:10.1016/j.soildyn.2020.106089.
- Ujjawal, K., H. Venkateswarlu, and A. Hegde. 2019. Vibration isolation using 3D cellular confinement system: A numerical investigation. *Soil Dynamics and Earthquake Engineering* 119:220–34. doi:10.1016/j.soildyn.2018.12.021.
- Wagner, P. R., V. K. Dertimanis, E. N. Chatzi, and J. L. Beck. 2018. Robust-to-uncertainties optimal design of seismic metamaterials. *Journal of Engineering Mechanics* 144 (3). doi:10.1061/(ASCE)EM.1943-7889.0001404.
- Wenzel, M., O. S. Bursi, and I. Antoniadis. 2020. Optimal finite locally resonant metafoundations enhanced with nonlinear negative stiffness elements for seismic protection of large storage tanks. *Journal of Sound and Vibration* 483:115488. doi:10.1016/j.jsv.2020.115488.
- Xiao L., Bursi O. S., Li H., Wang M. and Du X. (2023). Energy dissipation enhancement of flexural metamaterial beams with inerter and rotational deformation. *International Journal of Mechanical Sciences*, 237 107770 10.1016/j.ijmecsci.2022.107770
- Xiao L., Sun F. and Bursi O. S. (2020). Vibration Attenuation and Amplification of One-Dimensional Uncoupled and Coupled Systems with Optimal Metafoundations. *J. Eng. Mech.*, 146(7), 10.1061/(ASCE)EM.1943-7889.0001786

Appendices

A1. Dynamic stiffness

The dynamic stiffnesses of the springs that couple the foundation to the soil beneath are shown in Eq.(1). For clearance, Eq.(1) is repeated here.

$$S_j(a_0) = K_j(k_j(a_0) + ia_0c_j(a_0)) \quad (j = h, \theta) \tag{20}$$

a_0 is the dimensionless frequency which is equal to $\omega r_0/v_s$, where ω is the excitation frequency, and r_0 is the equivalent radius. The dynamic spring coefficients $k_j(a_0)$ and dynamic damping coefficients $c_j(a_0)$ ($j=h, \theta$) are calculated with

$$k_h(a_0) = 1 \tag{21}$$

$$c_h(a_0) = \frac{z_0 v_s}{r_0 v} \tag{22}$$

$$k_\theta(a_0) = 1 - \frac{1}{3} \frac{a_0^2}{\left(\frac{r_0 v}{z_0 v_s}\right)^2 + a_0^2} \tag{23}$$

$$c_\theta(a_0) = \frac{1}{3} \frac{z_0 v_s}{r_0 v} \frac{a_0^2}{\left(\frac{r_0 v}{z_0 v_s}\right)^2 + a_0^2} \tag{24}$$

The static stiffness K_j , the equivalent radius r_0 , the aspect ratio of the cone model z_0/r_0 , and the wave velocity v related to Poisson’s ratio ν with ($\nu \leq 1/3$) can be determined by the equations collected in Table A1 (Livaoglu 2008).

Table A1. Properties of cone models and static stiffness values of equivalent-circular foundation (Livaoglu 2008).

	Equivalent Radius r_0	Aspect Ratio z_0/r_0	Wave Velocity v	Static Stiffness
Horizontal	$\sqrt{\frac{ab}{\pi}}$	$\frac{\pi}{8}(2-\nu)$	v_s	$K_h = \frac{4Gr_0}{1-\nu}$
Rocking	$\sqrt[4]{\frac{a^3b}{3\pi}}$	$\frac{9\pi}{32}$	$2v_s$	$K_\theta = \frac{8Gr_0^3}{3(1-\nu)}$

Note: G: shear modulus; r_0 : radius of a circular foundation; ν : Poisson ratio.

A2. Free-field response

For a uniform layer of homogeneous soil overlying a rigid bedrock, harmonic horizontal motions of the bedrock produce vertically propagating shear waves in the soil. The soil layer is modeled as a linear-elastic material with a shear modulus G_s , shear wave velocity v_s and material damping ratio ξ_{soil} . The transfer function of the soil layer is easily derived from the one-dimensional wave propagation theory as:

$$R(i\omega) = \frac{u_{ff0}}{u_{g0}} = \frac{1}{\cos(qH)} \tag{25}$$

In Eq. (25), $q = \omega/v_s^*$ is the soil wavenumber, $v_s^* = v_s\sqrt{1+2i\xi_{soil}}$ is the complex-valued shear wave velocity of the soil, and ω is the cyclic frequency of excitation. u_{ff0} and u_{g0} denote the amplitudes of displacement of the top and bottom surface of the soil layer, respectively. H is the thickness of the soil layer.

A3. System matrices of the controlled system

The system matrices of the controlled systems with a n-cell metafoundation are presented here. In the case of the test model, $n = 3$.

$$\mathbf{m} = [m_1 \ m_1 \ \dots \ m_1 \ m_2 \ m_2 \ \dots \ m_2 \ m^i \ m_t \ m_{tr}]_{2n+3}^T \tag{26}$$

$$m_t = \sum_1^n (m_1 + m_2) + m^i \tag{27}$$

$$m_{tr} = \sum_1^n (m_1 h_j + m_2 h_j) + m^i h_{n+1} \tag{28}$$

$$m_{tr2} = \sum_1^n (m_1 h_j^2 + m_2 h_j^2) + m^i (h_{n+1})^2 \tag{29}$$

$$\mathbf{M}^{con} = \begin{bmatrix} \mathbf{M} & \mathbf{m}_b^T & \mathbf{m}_r^T \\ \mathbf{m}_b & m_t & m_{tr} \\ \mathbf{m}_r & m_{tr} & m_{tr2} \end{bmatrix} \tag{30}$$

$$\mathbf{m}_b = [m_1 \ m_1 \ \dots \ m_1 \ m_2 \ m_2 \ \dots \ m_2 \ m^i]_{2n+1} \tag{31}$$

$$\mathbf{m}_r = [m_1 h_1 \ m_1 h_2 \ \dots \ m_1 h_n \ m_2 h_1 \ m_2 h_2 \ \dots \ m_2 h_n \ m^i h_{n+1}]_{2n+1} \tag{32}$$

$$\mathbf{M} = \begin{bmatrix} \mathbf{M}^f & \mathbf{0} & \mathbf{0} \\ \mathbf{0} & \mathbf{M}^r & \mathbf{0} \\ \mathbf{0} & \mathbf{0} & \mathbf{M}^i \end{bmatrix}_{(2n+1) \times (2n+1)} \tag{33}$$

$$\mathbf{M}^f = \text{diag}(m_1, m_1, \dots, m_1)_{n \times n} \tag{34}$$

$$\mathbf{M}^r = \text{diag}(m_2, m_2, \dots, m_2)_{n \times n} \tag{35}$$

$$\mathbf{M}^i = m^i \tag{36}$$

$$\mathbf{K}^{con} = \begin{bmatrix} \mathbf{K}_1 & \mathbf{0} & \mathbf{0} \\ \mathbf{0} & K_h & \mathbf{0} \\ \mathbf{0} & \mathbf{0} & K_\theta \end{bmatrix} \tag{37}$$

$$\mathbf{K}_1 = \begin{bmatrix} \mathbf{K}^f + \mathbf{K}^r + \mathbf{K}_2^i & -\mathbf{K}^r & -(\mathbf{K}_2^i)^T \\ -\mathbf{K}^r & \mathbf{K}^r & \mathbf{0} \\ -\mathbf{K}_2^i & \mathbf{0} & \mathbf{K}_3^i \end{bmatrix}_{(2n+1) \times (2n+1)} \tag{38}$$

$$\mathbf{K}^f = \begin{bmatrix} k_1 & -k_1 & 0 & \dots & 0 \\ -k_1 & 2k_1 & \ddots & \ddots & \vdots \\ 0 & \ddots & \ddots & \ddots & 0 \\ \vdots & \ddots & \ddots & 2k_1 & -k_1 \\ 0 & \dots & 0 & -k_1 & k_1 \end{bmatrix}_{n \times n} \tag{39}$$

$$\mathbf{K}^r = \text{diag}(k_2, k_2, \dots, k_2)_{n \times n} \tag{40}$$

$$\mathbf{K}_1^i = \text{diag}(0, 0, \dots, 0, k^i)_{n \times n} \tag{41}$$

$$\mathbf{K}_2^i = [0, \dots, 0, k^i]_{1 \times n} \tag{42}$$

$$\mathbf{K}_3^i = k^i \tag{43}$$

$$\mathbf{C}^{con} = \begin{bmatrix} \mathbf{C}_1 & \mathbf{0} & \mathbf{0} \\ \mathbf{0} & C_h & \mathbf{0} \\ \mathbf{0} & \mathbf{0} & C_\theta \end{bmatrix} \tag{44}$$

$$\mathbf{C}_1 = \begin{bmatrix} \mathbf{C}^f + \mathbf{C}^r + \mathbf{C}_1^i & -\mathbf{C}^r & -(\mathbf{C}_2^i)^T \\ -\mathbf{C}^r & \mathbf{C}^r & \mathbf{0} \\ -\mathbf{C}_2^i & \mathbf{0} & \mathbf{C}_3^i \end{bmatrix}_{(2n+1) \times (2n+1)} \quad (45)$$

$$\mathbf{C}^f = \alpha_1 \mathbf{M}^f + \alpha_2 \mathbf{K}^f \quad (46)$$

$$\mathbf{C}^r = \text{diag}(c_2, c_2, \dots, c_2)_{n \times n} \quad (47)$$

$$\mathbf{C}_1^i = \text{diag}(0, 0, \dots, 0, c^i)_{n \times n} \quad (48)$$

$$\mathbf{C}_2^i = [0, \dots, 0, c^i]_{1 \times n} \quad (49)$$

$$\mathbf{C}_3^i = c^i \quad (50)$$